INTERNATIONAL JOURNAL OF CLIMATOLOGY
Int. J. Climatol. (2017)
Published online in Wiley Online Library
(wileyonlinelibrary.com) DOI: 10.1002/joc.5034

RMetS
Royal Meteorological Society

High-resolution regional-coupled ocean–atmosphere simulation of the Indian Summer Monsoon

Vasubandhu Misra,[a,b,c]* Akhilesh Mishra[a,c] and Amit Bhardwaj[a,c]

[a] *Center for Ocean-Atmospheric Prediction Studies, Florida State University, Tallahassee, USA*
[b] *Department of Earth, Ocean and Atmospheric Science, Florida State University, Tallahassee, USA*
[c] *Florida Climate Institute, Florida State University, Tallahassee, USA*

ABSTRACT: A 23-year integration of a Regional-Coupled Ocean–Atmosphere Model (RCOAM) centred over the Indian monsoon region is validated with observations and analysis for its seasonal climatology, evolution, and variability at intraseasonal and interannual scales. The RCOAM has the Regional Spectral Model (RSM) as its atmospheric component and Regional Ocean Model System (ROMS) as its oceanic component. They are both coupled at 15 km grid spacing with identical grids, without applying any form of flux correction and are forced with global fields of atmospheric and oceanic reanalysis. The verification indicates that the RCOAM simulation simulates the mean Indian Summer Monsoon (ISM) rainfall climatology and SST in the neighbouring oceans reasonably well with finer details apparent along the orography (e.g. Western Ghats, Himalaya) and along the upwelling regions of the coastal oceans. In addition the evolution of the ISM at its onset and its devolution around the time of demise in the RCOAM simulation both in the atmosphere and the ocean conform to its well known features and reinforce the coupled ocean–atmosphere phenomenon of the ISM. The intraseasonal variations in the RCOAM simulation also adhere to the observed composite of dry and wet spells of the ISM, with the low-level flow in the latter (former) counteracting (enhancing) the low-level atmospheric ISM climatological flow. The interannual variations in relation to the remote ENSO variations are also validated with respect to the observations. It is also shown that the variations of the length of the ISM to the seasonal anomalies of the ISM both in the RCOAM simulation and observations is largely a result of the ENSO teleconnection. However, significant systematic bias in surface fluxes, cloud fraction, SST, and precipitation of the RCOAM simulation of the ISM is also noted.

KEY WORDS monsoon; regional model; ENSO

Received 5 October 2016; Revised 13 December 2016; Accepted 22 January 2017

1. Introduction

The Indian Summer Monsoon (ISM) is one of the most hydro-climatically robust seasonal phenomenon on this planet with over 900 mm of rainfall falling over the subcontinent in a period of 4 months between June to September. This is nearly 75% of the total annual rainfall that India receives typically. This strong seasonal rainfall variation is also accompanied by significant seasonal variations in large-scale temperature gradient (Rai Sircar and Patil, 1961; Yanai *et al.*, 1992), tropospheric winds and wind shear (Ananthakrishnan *et al.*, 1968; Webster *et al.*, 1998), upper ocean Ekman transport (Wyrtki, 1971; Schott and McCreary, 2001), distinct land-atmosphere (Delworth and Manabe, 1988; Webster *et al.*, 1998; Koster *et al.*, 2004; Bollasina and Ming, 2013) and air–sea interactions (Webster *et al.*, 1998; Wang *et al.*, 2005; Misra, 2008). There have been varied attempts to simulate this phenomenon that span from simple 2D models (Webster and Chou, 1980; Drbohlav and Wang, 2005; Bordoni and Schneider, 2008) to complex 3D models that include the general circulation and regional models (Gadgil and Sajani, 1998; VenkataRatnam *et al.*, 2009; Lucas-Picher *et al.*, 2011; Kim *et al.*, 2012; Misra and Li, 2013).

Several of the studies have evaluated the simulation of the ISM from Atmospheric Global Circulation Models (AGCMs) with prescribed SST (e.g. Sperber and Palmer, 1996; Gadgil and Sajani, 1998; Sperber *et al.*, 2001). In many of these studies there is an overwhelming conclusion that the AGCMs have a tendency to have a wet bias in the equatorial Indian Ocean and a dry bias over the Indian subcontinent. However, in the recent past there are several studies which highlight the importance of local air–sea feedback processes for successful simulation of the ISM (Wang *et al.*, 2005; Wu and Kirtman, 2005; Misra, 2008). This has led to a concerted effort to use Coupled ocean–atmosphere Global Circulation Models (CGCMs) for the simulation and prediction of the ISM (Kim *et al.*, 2012; Ramu *et al.*, 2016). However, even the CGCMs display a dry bias over the subcontinent, albeit slightly less than their uncoupled counterparts (Chaudhari *et al.*, 2013).

For many decades, however, a number of regional atmosphere modelling studies of the ISM forced with global atmospheric reanalysis has also been conducted with

* Correspondence to: V. Misra, Center for Ocean-Atmospheric Prediction Studies, Florida State University, 2000 Levy Avenue, Building A, Suite 292, Tallahassee, Florida 32306, USA. E-mail: vmisra@fsu.edu

Table 1. Outline of the physics in RSM.

Atmospheric model (RSM) physics	Reference
Deep convection	Moorthi and Suarez (1992)
Shallow convection	Tiedtke (1983)
Boundary layer	Hong and Pan (1996)
Land model	Ek *et al.* (2003)
Gravity wave drag	Alpert *et al.* (1988)
Long-wave radiation	Chou *et al.* (1996)
Short-wave radiation	Chou and Suarez (1994)

varied success (Bhaskaran *et al.*, 1996; Ji and Vernekar, 1997; VenkataRatnam and Krishna Kumar, 2005; Dash *et al.*, 2006; Saeed *et al.*, 2009, 2012; Umakant *et al.*, 2015). A reverberating message from many of these studies is that higher resolution of the regional atmospheric model provides a more realistic simulation of the ISM through better representation of the orography, land-ocean coastlines, vegetation cover, and land use. Obviously this regional atmospheric downscaling framework ignores air-sea coupling, which is often cited as an inherent feature of the ISM (Webster *et al.*, 1998; Wang *et al.*, 2005; Misra, 2008).

Comparatively, there have been fewer studies describing the ISM simulation from regional-coupled ocean–atmosphere models (Seo *et al.*, 2008, 2009; VenkataRatnam *et al.*, 2009; Samala *et al.*, 2013), which offer both relatively high-grid resolution as well as include the important air-sea feedback process. An encouraging sign from these studies is that air-sea coupling in the regional model seems to improve the simulation of the ISM, especially in the intraseasonal time scales. In this study, we describe the analysis of 18 years of continuous coupled simulation of a regional-coupled ocean–atmosphere model forced with global reanalysis of the atmosphere and the ocean at the lateral boundaries at a horizontal grid resolution of 15 km. In the following section we describe the regional model followed by the details of the model integration. In Section 4 we present the results followed by conclusions in Section 5.

2. Model description

The Regional-Coupled Ocean–Atmosphere Model (RCOAM) adopted for this study is the Regional Spectral Model-Regional Ocean Modeling System (RSM-ROMS; Li and Misra, 2014). The RSM and the ROMS are the atmospheric and the oceanic components of RCOAM. This model has been used for several other climate

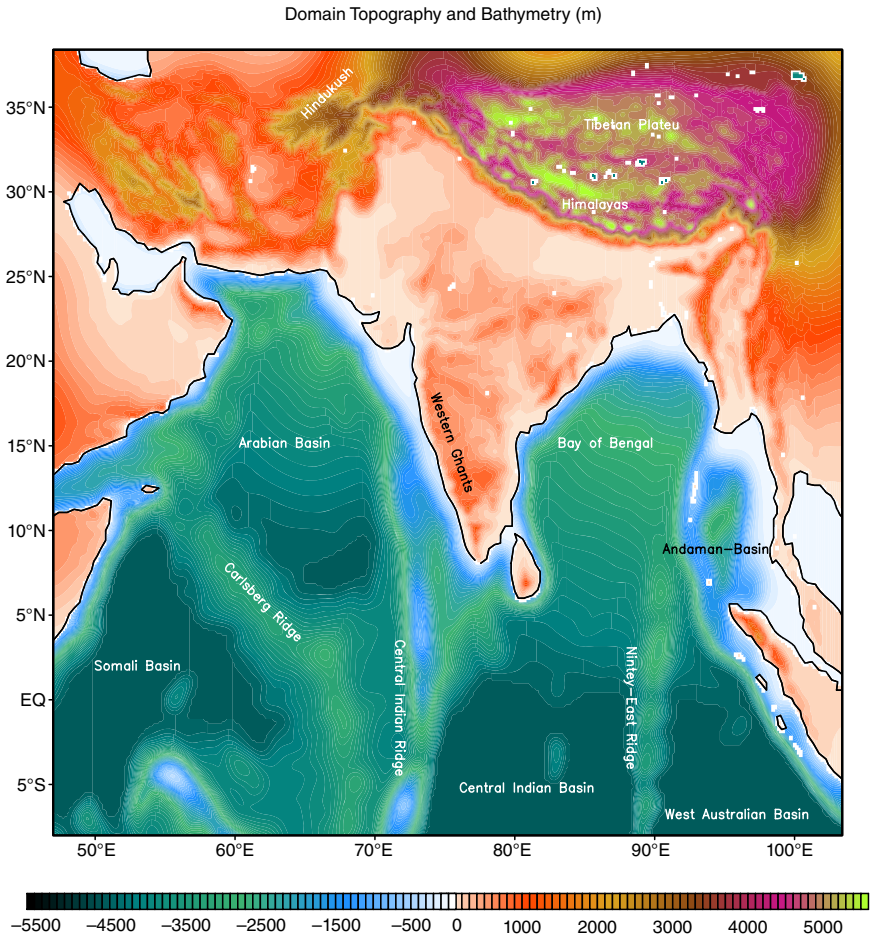

Figure 1. Domain of RCOAM overlaid with topography (m) over land and bathymetry (m) in ocean. [Colour figure can be viewed at wileyonlinelibrary.com].

Table 2. Differences of RCOAM simulation from other ISM studies using regional-coupled ocean–atmosphere climate model.

Model	Seo *et al.* (2008) RSM-ROMSv2.2	VenkataRatnam *et al.* (2009) RegCM3-ROMSv2.2	Samala *et al.* (2013) WRFv2.2-ROMSv2.2	Zou and Zhou (2016) RegCM3-LICOM2	RCOAM simulation RSM-ROMSv2.2
Horizontal resolution of regional atmosphere model (RAM)	0.26° × 0.26°	60 × 60 km	30 × 30 km	50 × 50 km	15 × 15 km
Horizontal resolution of regional ocean model (ROM)	0.26° × 0.26°	60 × 60 km	10 × 10 km	Variable meridional resolution from 0.5° to 1° and latitudinal grid spacing of 1°	15 × 15 km
Vertical discretization of RAM	28 sigma levels	16 sigma levels	28 sigma levels	18 sigma levels	28 sigma levels
Vertical discretization of ROM	20 sigma levels	24 sigma levels	24 sigma levels	30 vertical levels	30 sigma levels
Lateral boundary condition (LBC) for RAM	NCEP-DOE, Kanamitsu *et al.* (2002)	NCEP-NCAR, Kalnay *et al.* (1996)	NCEP-NCAR, Kalnay *et al.* (1996)	NCEP-DOE, Kanamitsu *et al.* (2002)	NCEP-DOE Kanamitsu *et al.* (2002)
LBC for ROM	Monthly Climatology for World Ocean Atlas, Conkright *et al.* (2002)	Monthly Levitus Climatology, Monterey and Levitus (1997)	Monthly Levitus Climatology, Monterey and Levitus (1997)	Not applicable	SODAv2.2.4, Carton and Giese (2008)
Use of flux correction	No	Surface salinity is specified from Levitus Climatology	Surface salinity is specified from Levitus Climatology	No	No
Use of flux coupler (i.e. flux recalculation at interface)	Yes, Seo *et al.* (2007)	No	No	Yes, Valcke (2006)	No
Coupling interval between RAM and ROM	1 day	1 day	6 h	1 day	1 day
Experiment design	14-year simulation (1993–2006)	Seasonal runs from 1 May to 30 September for years 1997, 1998, 2002, and 2003	Seasonal runs from 1 May to 30 September for years 2000 to 2007	Continuous integration for 23 years from 1988 to 2010	Continuous integration of 23 years from 1 January 1985 to 31 December 2007

Table 3. Verification datasets for model validation.

	Variable	Name of dataset (acronym used to identify dataset)	Spatial resolution of dataset	Temporal resolution of dataset	Available time period[a]	Source
1	Precipitation	Indian Meteorological Department (IMD)	0.25° × 0.25°	Daily	1900–2005	Pai *et al.* 2014
2	Precipitation	TRMM-3B43 (TRMM)	0.25° × 0.25°	Daily	1998–2015	Huffman *et al.* (1995); 1997; Adler *et al.* 2000
3	Tropospheric winds and temperature	Modern-Era Retrospective Analysis for Research and Applications, Version 2 (MERRA-2)	0.5° × 0.625°	Daily	1979–present	Suarez and Bacmeister (2015); Reichle and Liu (2014); Wargan and Coy (2016)
4	Upper air data (for lateral boundary conditions of RSM)	NCEP-R2	2.5° × 2.5°	6-h	1948–present	Kanamitsu *et al.* (2002)
5	Ocean currents and temperature	Climate Forecast System Reanalysis (CFSR)	0.5° × 0.5°	Daily	1979–present	Saha *et al.* 2010
6	Ocean temperature, salinity, and currents (for lateral boundary conditions for ROMS)	Simple Ocean Data Assimilation v2.2.4 (SODAv2.2.4)	0.25° × 0.4° × 40 levels	Monthly	1958–2001	Carton and Giese (2008)
7	SST	Optimum Interpolation Sea Surface Temperature Version 2 (OISSTv2)	0.25° × 0.25°	Daily	1990–2007	Reynolds *et al.* (2007)
8	SST	Operational Sea Surface Temperature and Sea Ice Analysis (OSTIA)	5 × 5 km	Daily	2006–2014	Donlon *et al.* (2011)
	Cloud fraction	International Satellite Cloud Climatology Project (ISCCP)	2.5° × 2.5°	Monthly	1983–2009	Rossow and Schiffer (1999)
	Ocean surface fluxes	Ocean–Atmosphere Flux (OAFLUX)	1° × 1°	Daily	1979–present	Yu *et al.* (2008)

[a]The validation period was made to overlap with the RCOAM period of simulation.

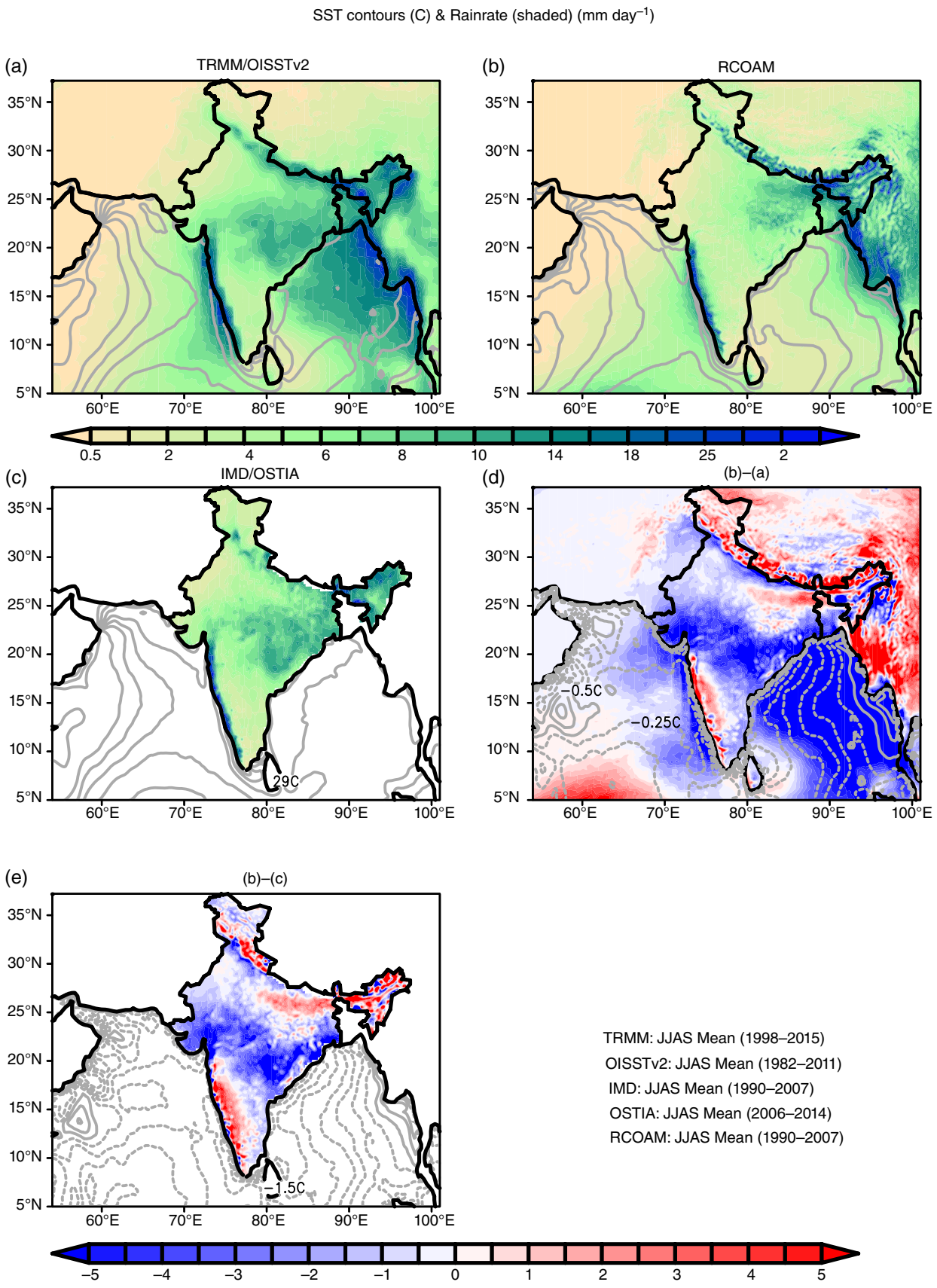

Figure 2. The seasonal mean JJAS climatology of SST (contoured; °C), rainfall (shaded; mm day^{-1}) from (a) the RCOAM simulation, (b) TRMM rainfall observations and OISSTv2, (c) IMD rainfall over land and OSTIA SST over ocean, (d) corresponding systematic errors of RCOAM simulation (a–b), and (e) corresponding systematic errors of RCOAM simulation b–c. [Colour figure can be viewed at wileyonlinelibrary.com].

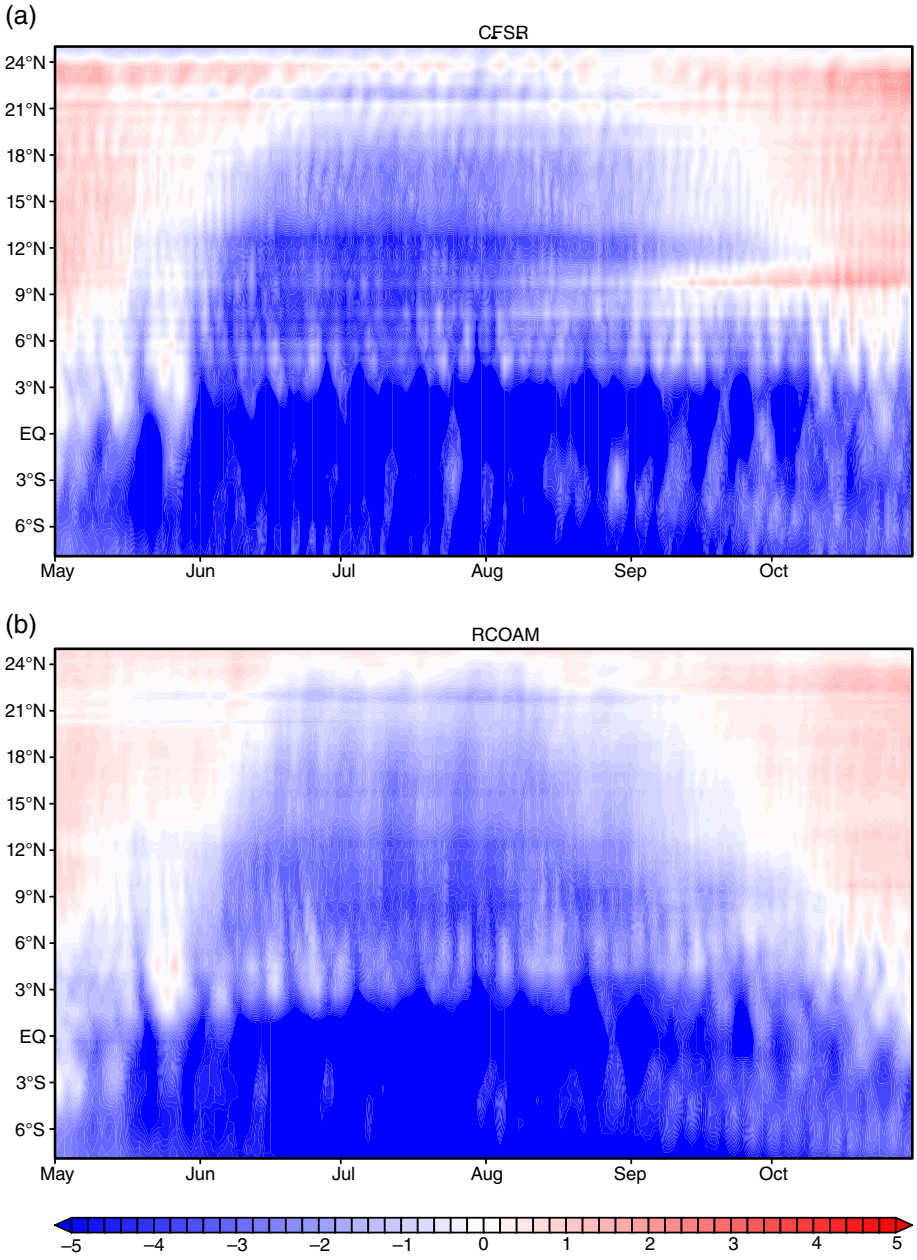

Figure 3. (a) The climatological daily meridional progression of zonally averaged meridional ocean heat transport computed to a depth of 20 °C isotherm from CFSR. Here, negative (positive) values refer to the southward (northward) heat transport. Units are in GigaWatts ($=10^9$ W). (b) Same as (a) but from the RCOAM simulation. [Colour figure can be viewed at wileyonlinelibrary.com].

simulation studies (e.g. Li *et al.*, 2012, 2013, 2014; Li and Misra, 2014; Misra *et al.*, 2016; Misra and Mishra, 2016). The RSM was first introduced in Juang and Kanamitsu (1994). It has since undergone several changes and revisions and its most current version is described in great detail in Kanamitsu *et al.* (2010). The RSM has 28 terrain following sigma vertical coordinates. An outline of the physics used in RSM for this study is provided in Table 1.

Similarly, ROMS version 3.0 uses 30 vertical sigma levels. This is a stretched terrain following (S) co-ordinate on a horizontal staggered Arakawa-C grid (Haidvogel *et al.*, 2000; Shchepetkin and McWilliams, 2005). The mixing scheme is a local closure scheme following the level 2.5 turbulent kinetic energy equations (Mellor and Yamada, 1982) and generic length scale parameterization of Umlauf and Burchard (2003). The boundary layer formulation follows Large *et al.* (1994), which is a nonlocal closure scheme based on the K-profile.

The RSM and ROMS in the RCOAM interact through the efficient Message Passing Interface (MPI) dual coupling scheme with a coupling interval of 24-h. It may be noted that the coupling interval could be raised to higher interval but is futile given the current vertical discretization in ROMS (with the first layer being 5 m thick) and mixing

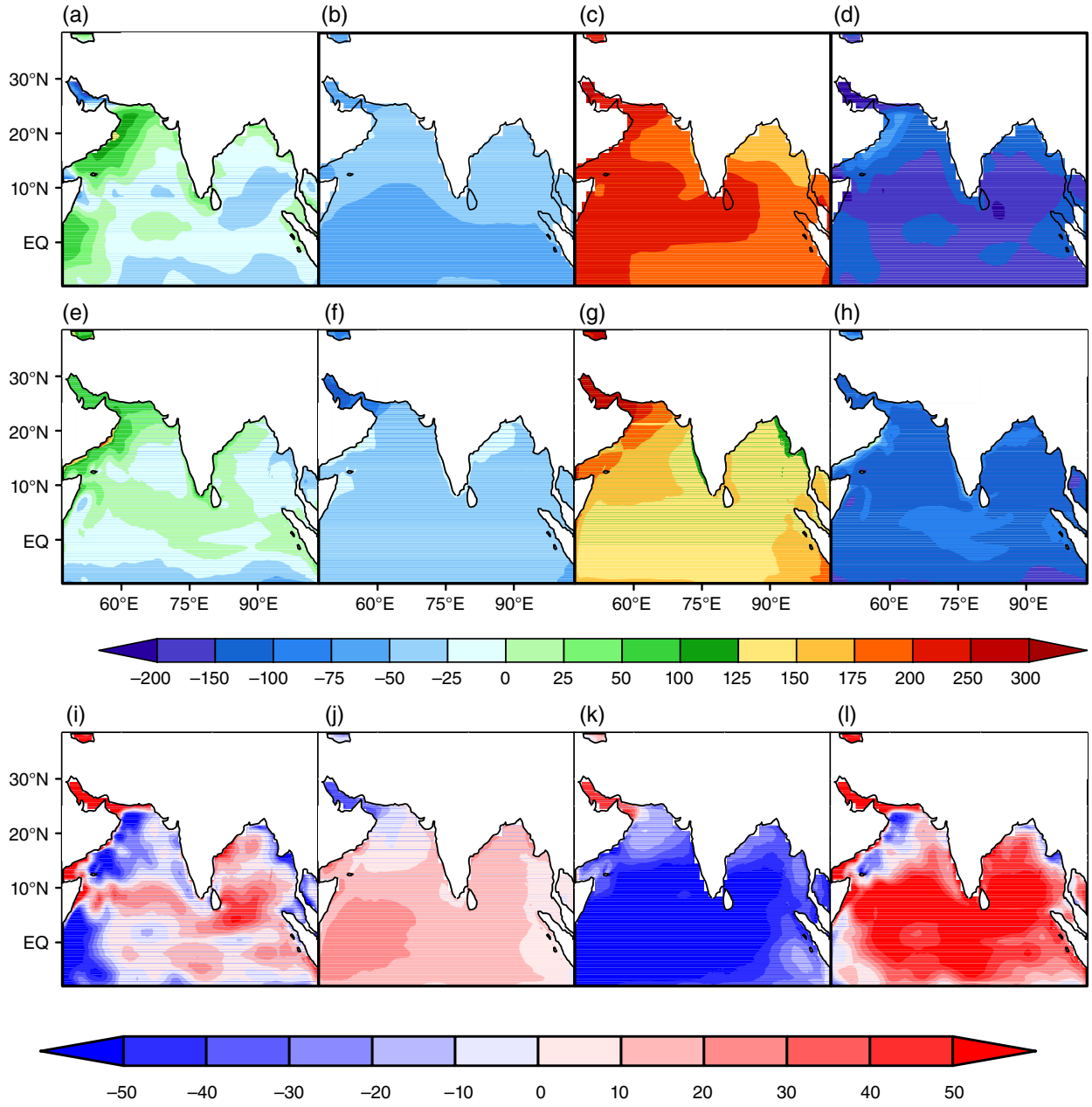

Figure 4. The climatological JJAS mean net (a) net heat, (b) long wave, (c) short wave, and (d) enthalpy (sensible and latent heat) fluxes from OAFLUX (see Table 3). (e–h) Same as (a–d) but from the RCOAM simulation. (i–l) Corresponding systematic errors of the RCOAM simulation. The units are in W m^{-2}. [Colour figure can be viewed at wileyonlinelibrary.com].

parameterization in ROMS to realize the benefits of say diurnal variations in air-sea coupling. The grid interval in RSM and ROMS is made identical so that they share the same land-ocean mask. Therefore the use of a flux coupler in the RCOAM is avoided. Therefore in the RCOAM there is a direct exchange of the daily mean atmospheric fluxes and SST between RSM and ROMS at the time of the coupling.

3. Details of model integration and verification datasets

The domain of the RCOAM with the topography over land and bathymetry over the ocean at 15 km grid resolution is shown in Figure 1. RCOAM is integrated from 1985 to 2007. The regional domain (Figure 1) is relatively large with 400×353 being the grid dimension in the x and y directions, respectively. Several of the ocean floor features including prominent ridges (e.g. Carlsberg, Central Indian, Ninetyeast Ridges) and basins (e.g. Somali, Arabian, Central Indian, Western Australian, and Andaman Basins) are resolved at this grid spacing and domain. The comparatively broad continental shelf on the western side of peninsular India relative to the narrower continental shelf along its eastern coast is also apparent. Similarly, several of the topographic features over land are also prominent in Figure 1 including the Tibetan Plateau, the Himalayas, the Hindukush mountains over Afghanistan, the Western

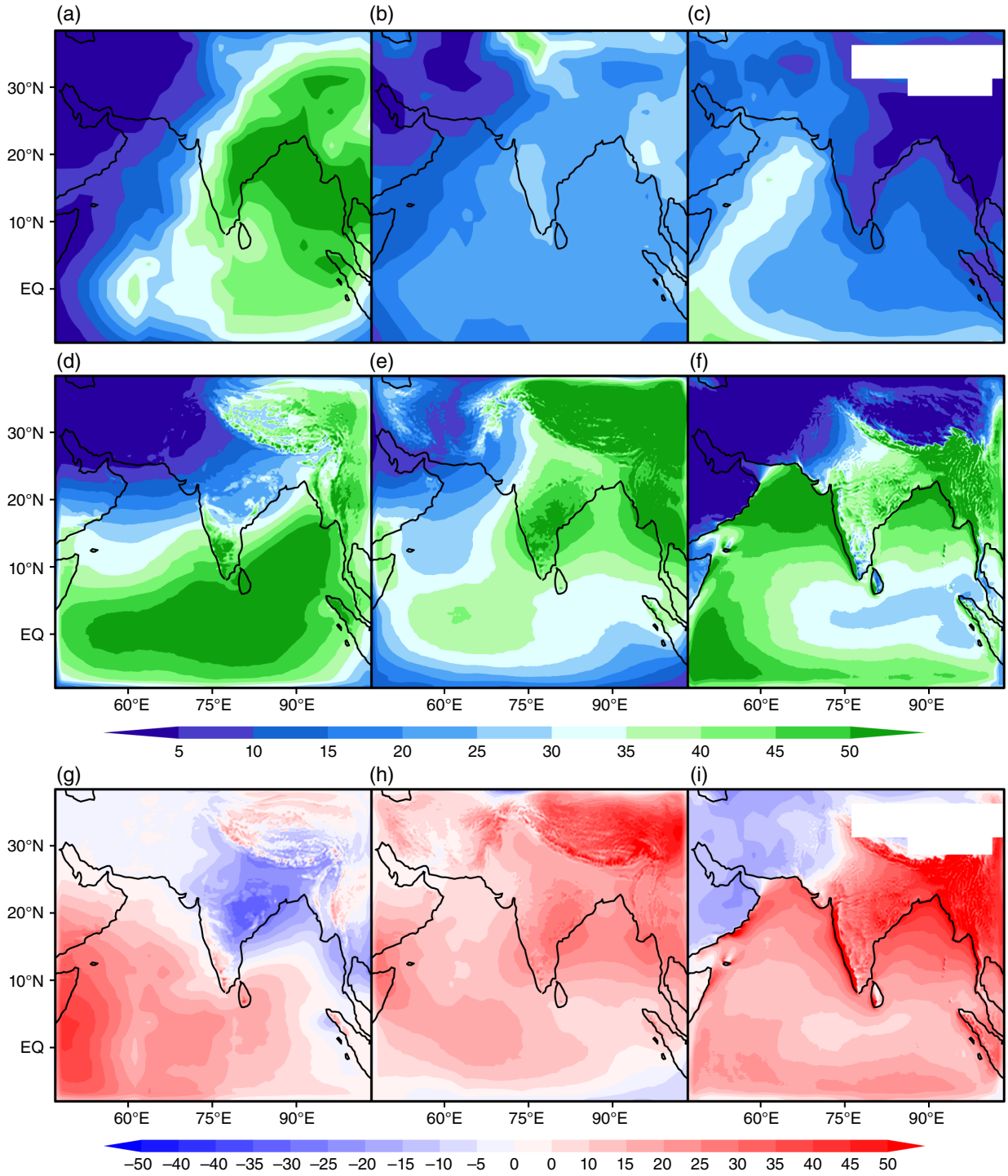

Figure 5. The climatological mean JJAS (a) high, (b) medium, (c) low cloud fraction from ISCCP (see Table 3). The corresponding (d) high, (e) medium, and (f) low cloud fraction from RCOAM simulation. The corresponding systematic errors of the RCOAM simulation for (g) high, (h) medium, and (i) low cloud fraction. [Colour figure can be viewed at wileyonlinelibrary.com].

Ghats, and the appearance of fishbone-like structure of several mountain ranges across the central part of India.

RCOAM is laterally forced by National Centers for Environmental Prediction-Department of Energy (NCEP-DOE) global atmospheric reanalysis (Kanamitsu *et al.*, 2002) and Simple Ocean Data Assimilation v2.2.4 (SODA) global oceanic analysis (Carton and Giese, 2008) for the atmospheric (RSM) and oceanic (ROMS) components, respectively. NCEP-DOE reanalysis is available at 2.5° grid spacing and SODA reanalysis is available at 0.5° grid spacing. The lateral boundary forcing to RSM is applied at interval of 6 h and ROMS is laterally forced by the monthly SODA oceanic boundary conditions (temperature, salinity, ocean currents). Although the RCOAM integration is 23 years long (1985–2007), we have neglected the first 5 years (1985–1989) of

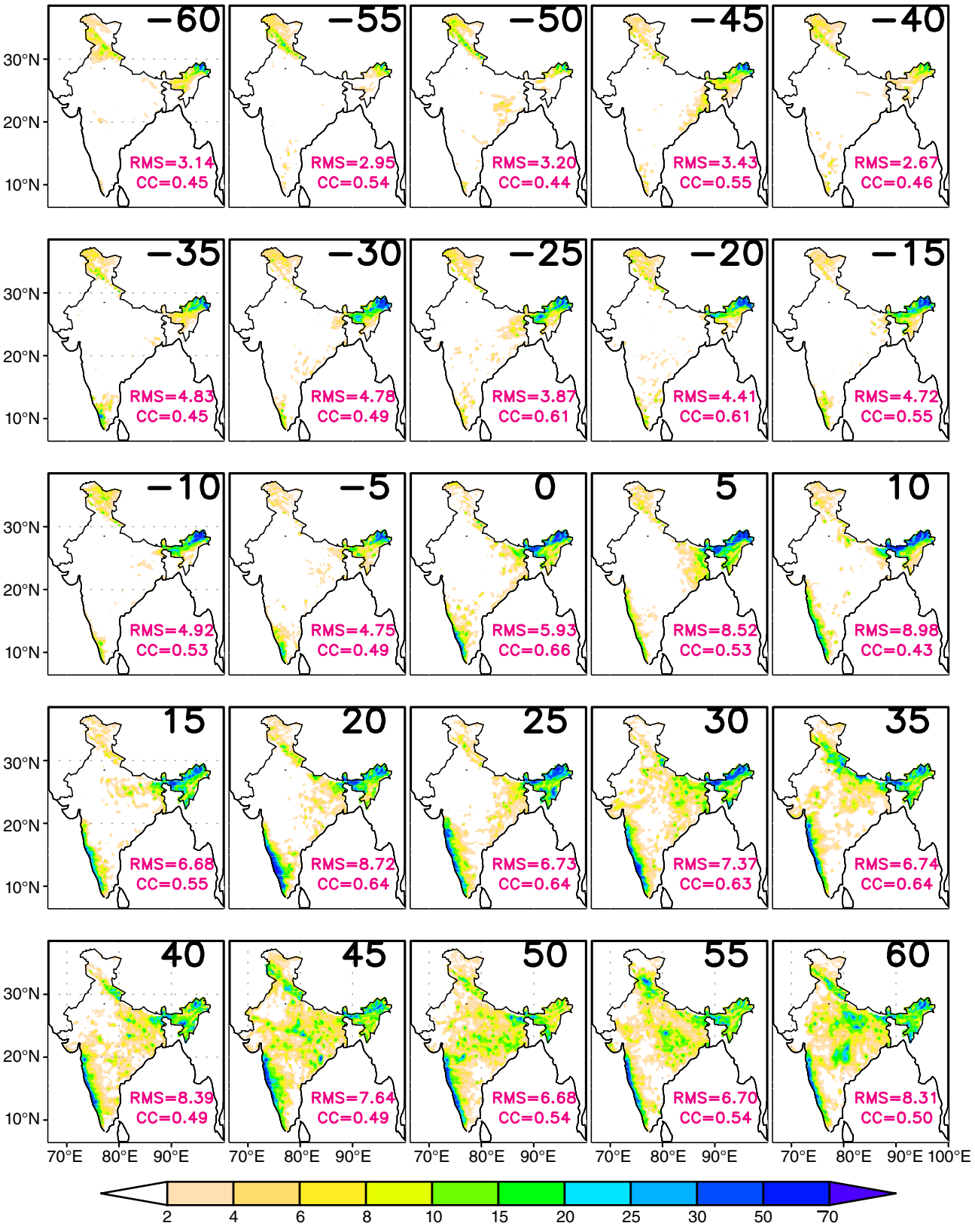

Figure 6. The climatological progression of RCOAM rainfall prior, at, and post-onset of the ISM. The spatial correlations (CC) and the root mean square error (RMS; mm day^{-1}) of this progression with corresponding climatological progression from IMD rainfall dataset is indicated in each panel. [Colour figure can be viewed at wileyonlinelibrary.com].

the RCOAM simulation to account for ocean spin-up, which was initiated with initial conditions from SODA reanalysis that was interpolated to the RCOAM grid. In many aspects, the RCOAM simulation is rather unique in comparison to the minority of studies conducted on the ISM using a regional-coupled ocean–atmosphere model (Table 2). For example, the length of the RCOAM integration, its high horizontal resolution, use of realistic boundary conditions and avoidance of any flux correction is unique to this study relative to other comparable regional-coupled ocean–atmosphere modelling studies of the ISM (Table 2). Many of these other studies either employ monthly climatological fields of temperature and salinity as boundary forcing for ROMS and or use some form of nudging at surface to avoid drift of surface salinity, temperature. In other instances the horizontal resolution is more than twice as large as RCOAMS or the vertical resolution of the atmosphere and or ocean is coarser than RCOAMS.

The verification datasets used to validate the RCOAM simulation in this study is listed in Table 3. It may be noted that where possible (or available), the period of the observations or analysis (Table 3) was chosen to overlap with the validation period of the RCOAM simulation (1990–2007). Although RCOAM simulation is forced by NCEP-DOE reanalysis, the upper air variables are validated with MERRA-2, a more modern reanalysis that incorporates improvements in the model, newer satellite retrieved datasets are assimilated, and is available at higher resolution (Kim *et al.*, 2014). Similarly, for the same reasons we use CFSR to validate oceanic variables as opposed to SODA reanalysis that is used to force the RCOAM simulation. In addition, Goswami and Sengupta (2003) indicate that NCEP renanalysis severely underestimates the intraseasonal wind variations of the ISM and they attribute this to the bias in precipitation of the reanalysis.

4. Results

4.1. Seasonal climatology

Figure 2(a) shows the June–July–August–September (JJAS) mean rainfall and SST climatology from TRMM and OISSTv2. The corresponding climatology from the RCOAM simulation is shown in Figure 2(b) and the systematic errors in Figure 2(d). It is clear from these three panels that the RCOAM simulation is underestimating rainfall over a large transect over central India and over estimating rainfall over high terrain (e.g. northeastern India, western Ghats, and over southeast Asia). This is also accompanied by underestimation of SST over the Bay of Bengal, the Arabian Sea, and the equatorial Indian Ocean. Ironically, however, if the systematic errors of the RCOAM simulation is examined with respect to the gridded, rain gauge-based analysis of the Indian Meteorological Department (Pai *et al.*, 2014; Figure 2(c) and (e)) then the observational uncertainty of the ISM rainfall climatology is apparent. For example, the dry bias over northwestern parts (e.g. Rajasthan, Punjab, Delhi) and across to the eastern parts (e.g. West Bengal, Orissa, Jharkhand) of India in Figure 2(d) are far less severe in Figure 2(e). Similarly the wet bias over high terrain (e.g. western Ghats, Jammu and Kashmir, northeastern India) in Figure 2(d) are less extensive and even changes sign in some regions in Figure 2(e). It is well known that rainfall retrieved from TRMM is relatively more uncertain over high terrain regions (Dinku *et al.*, 2010; Ward *et al.*, 2011; Zulkafli *et al.*, 2014). More fundamentally, these observational uncertainties in gauge-based and radar-based estimates can be traced to the different character of the measurements: gauges give a point estimate of rain rate while radar estimate provide a volume averaged rain rate (Zawadzki, 1975; Habib and Krajewski, 2002). It should, however, be noted that while the IMD rainfall climatology period overlaps with the RCOAM simulation period, the TRMM observational period covers between 1998 and 2015, which partially covers the RCOAM simulation period. This also contributes to some of the differences in the observed climatology between TRMM and IMD rainfall datasets, given the potential contribution of the variations over the time period to the climatology.

Similarly, the systematic errors of SST from the RCOAM simulation in Figure 2(c) is greatly modulated, when we replace the OISSTv2 with the Met Office Operational SST and Sea Ice Analysis System (OSTIA; Donlon *et al.*, 2011; Figure 2(c) and (e)), which is available at 5 km grid spacing at daily interval. Once again, the cold SST bias in Figure 2(d) of the RCOAM simulation is enhanced over the Bay of Bengal, the Arabian Sea, and over the equatorial Indian Ocean using OSTIA (Figure 2(e)). The differences in the SST analysis products in Figure 2(a) and (c) arise from a multitude of reasons including the disparate spatial resolutions (see Table 3), the use of additional satellite retrieved products used in OSTIA, and differences in the analysis procedure where different weights are given to SST retrievals (Reynolds *et al.*, 2010). Furthermore, the differences can also arise from the fact that climatology of the two SST analysis products are derived from two different periods: OISSTv2 is over 1990–2007 while it is 2006–2015 for the OSTIA. It may be noted that northern Indian Ocean is shown to display decadal variations of the upper ocean (Han *et al.*, 2014) that may account for some of the differences between OISSTv2 and OSTIA.

Figure 3 shows the climatological upper ocean heat transport (given below by Equation (1)) as a function of latitude and day of the season.

$$\overrightarrow{H} = \int_{z_{20c}}^{z_{\text{surface}}} \overrightarrow{V} T C_w \rho_w dz \tag{1}$$

where $\overline{V}$ is the ocean current, T is the ocean temperature (in K), C_w (=3850 J kg^{-1} K^{-1}) and ρ_w (=1025 kg m^{-3}) are heat capacity and density of sea water, and Z_{20C} is the depth of the 20 °C isotherm. As pointed in earlier studies, the Ekman ocean heat transport plays an important role in the energy balance of the ISM as it transports as much heat from the northern to the southern Indian Ocean as

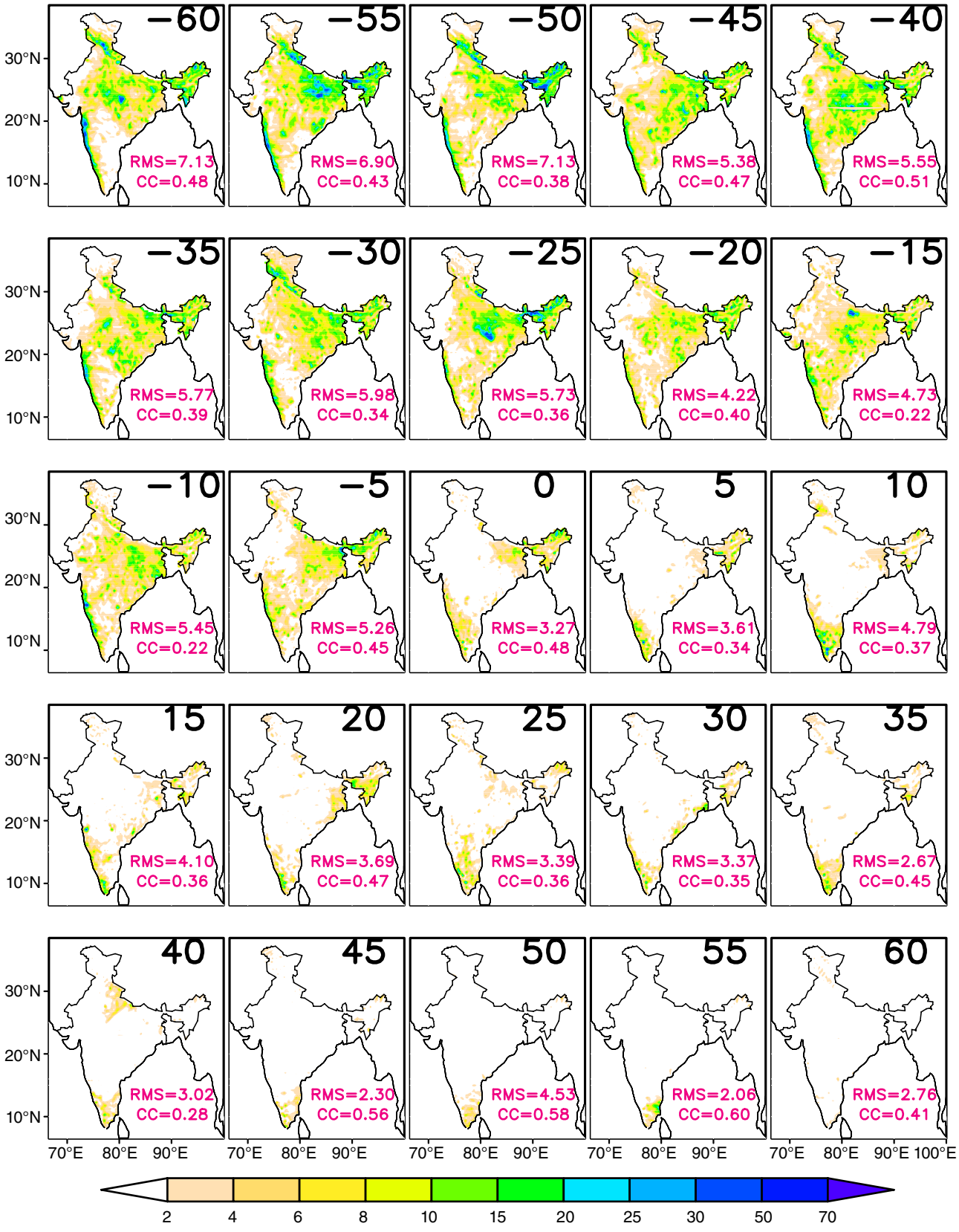

Figure 7. Same as Figure 6 but for rainfall prior, at, and post-demise of the ISM. [Colour figure can be viewed at wileyonlinelibrary.com].

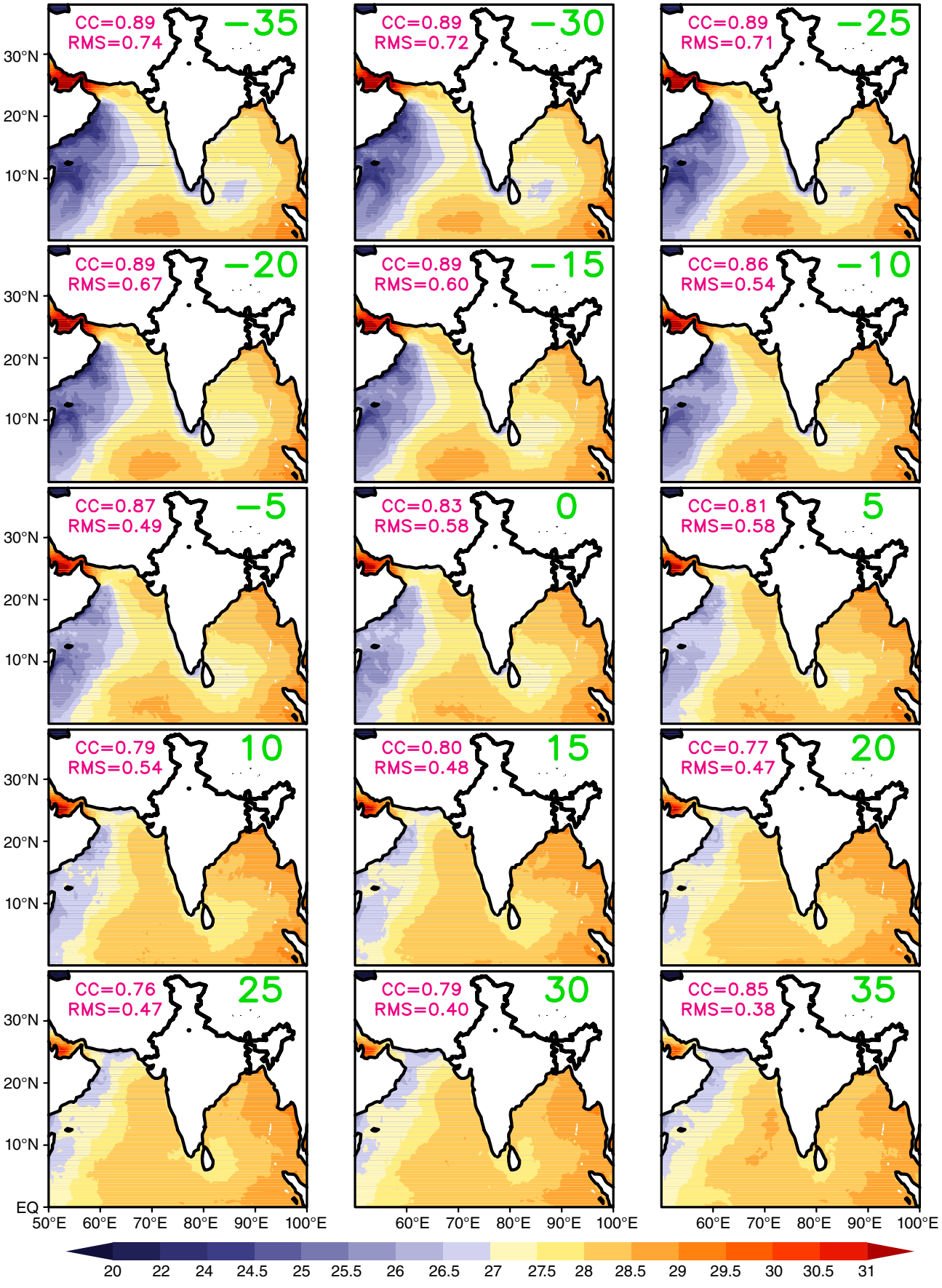

Figure 8. Same as Figure 6 but for SST. The spatial correlations (CC) and root mean square error (RMS; °C) are with respect to OISSTv2. [Colour figure can be viewed at wileyonlinelibrary.com].

the atmosphere transports heat from the southern to the Northern Indian Ocean (Webster, 2000; Chirokova and Webster, 2006). In Figure 3(a) and (b), we clearly see that the ocean heat transport rapidly transitions from northward (positive) to southward (negative) by mid-June (coinciding with climatological onset date of ISM of around June 1) from equatorial latitudes to 21°N both in the CFSR and in the RCOAM simulation. This southward transport remains rather steady across these latitudes till the demise of the season, when the ocean heat transport gradually reverts to northward transport across these northern latitudes of the Indian Ocean by end of October (Figure 3(a) and (b)). The RCOAM simulation nicely captures this robust feature of the ISM (Figure 3(b)), although the magnitude of the transport north of the equator is underestimated relative to the CFSR reanalysis (Figure 3(b)).

The JJAS mean climatological net surface heat flux and its components from the observational analysis (Table 3) is shown in Figure 4(a)–(d). In the ISM season, there is a relatively large net (positive) heat flux entering the ocean along the western boundary (e.g. east African coast, coast of Oman) and along the coastal region of India. In other parts of the ocean in the domain (e.g. central Bay of Bengal, central Arabian Sea) there is net (negative) surface heat flux leaving the ocean surface. This pattern fits well with the cold upwelling regions receiving more net short-wave radiation (Figure 4(c)) that is partially compensated by the upwelling long wave (Figure 4(b)) and enthalpy (Figure 4(d)) fluxes leaving the ocean surface. The corresponding fluxes from the RCOAM simulation (Figure 4(e)–(h)) also conform to a similar pattern with the upwelling regions and the coastal regions of the ocean surface around India receiving more net heat flux at surface from the atmosphere, while the majority of the other open ocean area (with exception over equatorial central Indian Ocean) losing heat to the atmosphere. However, the magnitudes of the bias (Figure 4(i)–(l)) indicate that the heat received in the upwelling and coastal regions by the ocean surface in the RCOAM simulation is less while the heat retained by the ocean surface in the open ocean is more than the observed analysis. This stems from a systematic bias of underestimating short-wave flux (Figure 4(k)), underestimating the upwelling long-wave flux (Figure 4(j)) and the enthalpy flux (Figure 4(l)). As a result of these compensatory effects the bias of the net heat flux in the RCOAM simulation (Figure 4(i)) is far less than in its individual components (Figure 4(j)–(l)).

The underpinnings of this bias in surface fluxes are also reflected in the bias of the cloud fraction in the RCOAM simulation (Figure 5). We have compared the high, low, and middle clouds of the simulation with the International Satellite Cloud Climatology Product (ISCCP) D2 (see Table 3) in Figure 5. This comparison shows that the RCOAM simulation overestimates (underestimates) the high clouds in the Arabian Sea and in the western Indian Ocean (over the subcontinent; Figure 5(a), (d), and (g)). The RCOAM simulation overestimates the middle (Figure 5(b), (e), and (h)) and the low (Figure 5(c), (f), and (i)) clouds across the domain except in the northwest regions of the domain where the simulation underestimates the low cloud fraction (Figure 5(i)) relative to the ISCCP.

4.2. Onset and demise of the monsoon

The evolution of the onset and demise of the ISM is rather pronounced in the seasonal evolution of the ISM (Koteswaram, 1958; Krishnamurti and Ramanathan, 1982; Ananthakrishnan and Soman, 1988). Noska and Misra (2016) introduced an objective criterion of defining onset and demise of the ISM based on the all India average daily rainfall. They found that onset (demise) day of the ISM coincides with first (last) day when the daily cumulative anomalies (computed relative to the annual mean climatology) of the all India averaged rainfall reaches a minimum (maximum) for the year. In Figure 6, we show the composite evolution of the daily rainfall 60 days before (day −60) and after (day 60) the onset date (day 0) of the ISM. The corresponding RMS error and spatial correlation of the climatology from the RCOAM simulation with the corresponding climatology from the IMD rainfall dataset is also indicated. As noted in Figure 6 and akin to the observational analysis in Noska and Misra (2016), the onset evolution is characterized by sustained heavy rainfall ($\sim$10–20 mm day^{-1}) over parts of northeastern India prior to the onset date of the ISM. But the southwestern (Malabar) coast witness a moderate rise in rain rate about 5 days prior to the onset date that continues to rise almost 20 days after the onset date. The RMS error ostensibly also grows post-onset with the rise in rainfall compared with pre-onset period. The spatial correlation of the rainfall from the RCOAM simulation with the IMD rainfall over this 120-day period (Figure 6) is around 0.5 suggesting a potential large-scale forcing (investigated further later) that gives rise to this reasonable simulation of the spatial precipitation pattern centred around the evolution of the onset of the ISM. The corresponding devolution of the ISM centred around the demise date is shown in Figure 7. Unlike the evolution of the ISM around the onset date, the spatial correlation of the RCOAM simulation with IMD rainfall is comparatively lower. However, the RMS error is lower around the demise period (Figure 7) owing to lower climatological rainfall than at the time of the onset (Figure 6). The demise of the ISM is characterized by the receding of the rainfall across India including in the northeastern and southwestern parts of the subcontinent, albeit after the demise date of the ISM in the latter areas (Figure 7; cf. Figure S4 in Noska and Misra, 2016).

A similar evolution of SST in the RCOAM simulation centred around the time of the onset of the ISM is shown in Figure 8. The spatial correlations with corresponding OISSTv2 are generally very high through the evolution (Figure 8). However, the domain averaged RMS error is nearly 1.1 °C throughout the simulation, which to some extent is on account of the discrepancy in the coastal SST (Figure 2). This discrepancy arises partly because of the comparatively coarse resolution of OISSTv2 relative to the RCOAM simulation with the former unable to resolve strong SST gradients (Figure 2). The sustained

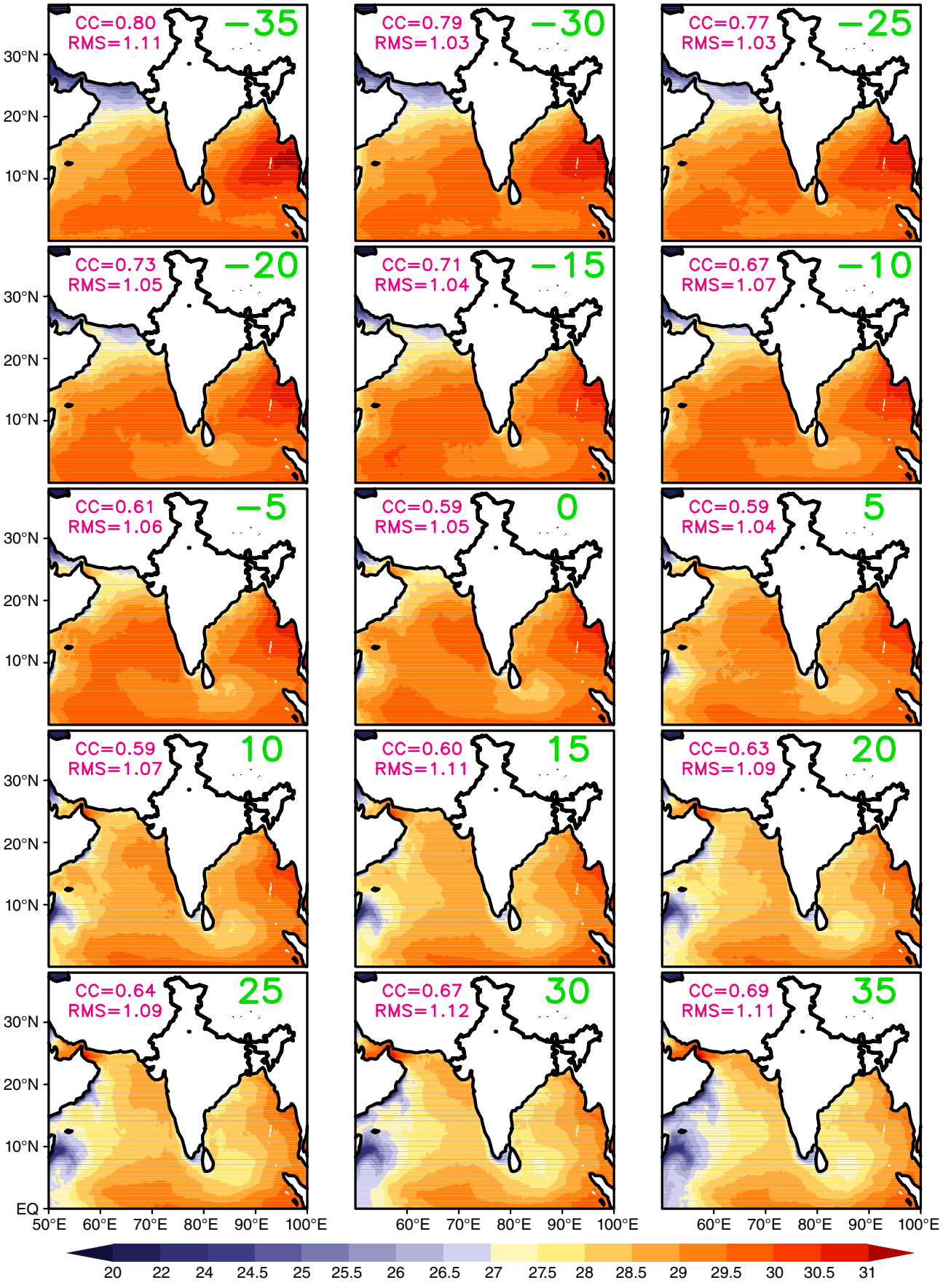

Figure 9. Same as Figure 6 but for SST prior, at, and post-demise of the ISM. [Colour figure can be viewed at wileyonlinelibrary.com].

Figure 10. Same as Figure 6 but for 850 hPa kinetic energy. The spatial correlations (CC) and root mean square error (RMS; m^2s^{-2}) are with corresponding climatological progression of the 850 hPa kinetic energy in units of m^2s^{-2} from MERRA2. [Colour figure can be viewed at wileyonlinelibrary.com].

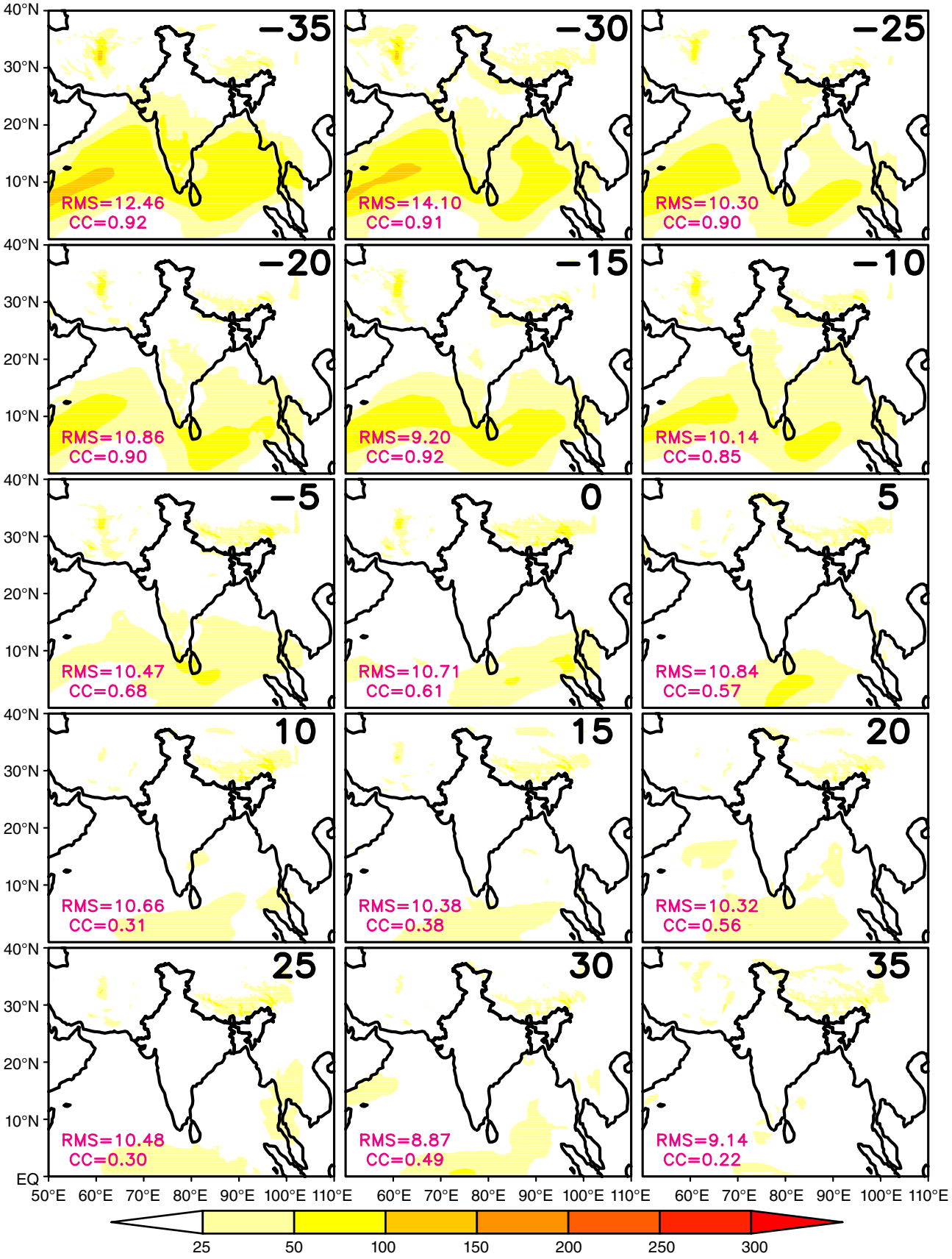

Figure 11. Same as Figure 6 but for 850 hPa kinetic energy prior, at, and post-demise of the ISM. The spatial correlations (CC) and root mean square error (RMS; m^2s^{-2}) are with corresponding climatological progression of the 850 hPa kinetic energy in units of m^2s^{-2} from MERRA2. [Colour figure can be viewed at wileyonlinelibrary.com].

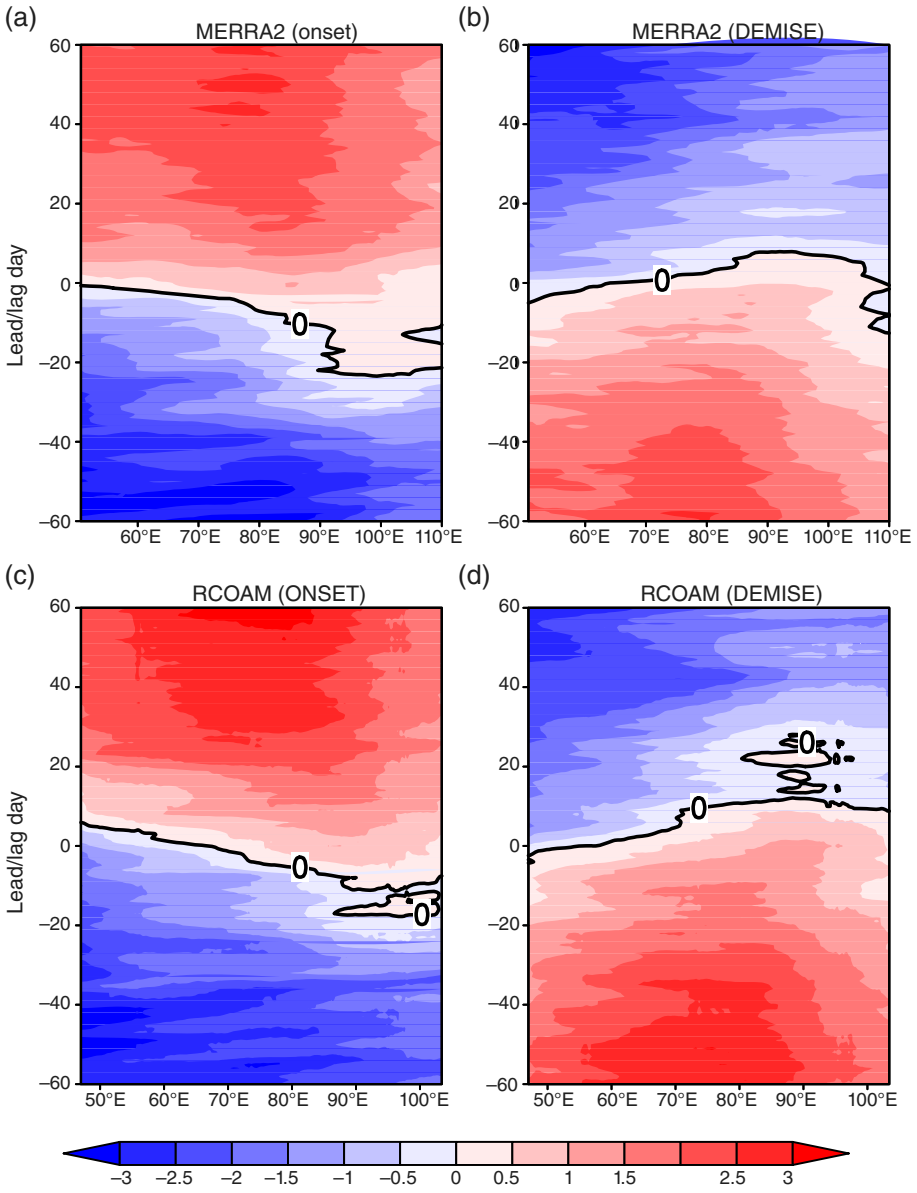

Figure 12. (a) The climatological daily zonal progression of the meridional temperature gradient between 5° and 25°N at 300 hPa from MERRA-2 as a function of lead/lag time with respect to onset date of the ISM from 40° to 120°E derived from IMD from observations. Here, negative (positive) values on the *y*-axis refer to the meridional temperature gradient leading (lagging) the onset date. Units are in °C 1000 km^{-1}. (b) Same as (a), but centred on the demise date. (c) Same as (a) but from RCOAM. (d) Same as (b) but from RCOAM. [Colour figure can be viewed at wileyonlinelibrary.com].

warm SST's (>30 °C) in eastern Bay of Bengal (centred over the Andaman Basin) in the pre-onset period (day −35 to day −5) and thereafter its cooling and receding of the warm SST further east is apparent in the evolution. In addition, the cooling of the Arabian SST just prior to onset of the ISM (from day −5 to day 0) and then its subsequent further cooling is also captured in the simulation.

Similarly, the devolution of the SST's centred around the demise of the ISM (Figure 9) indicates a rapid cooling prior to the demise. This originates from the strong cooling associated with the coastal upwelling along the coast of Somalia, which gradually spreads eastward. However, just prior to (∼day −5) and after the demise date (day 0), the rate of cooling along the coast of Somalia subsides, while the rest of the Indian Ocean in the domain begins to warm (Figure 9). It may be noted that unlike the evolution around the onset, the SST simulation around the demise date of the ISM has a lower spatial correlation with OISSTv2. But the RCOAM simulation also displays a lower RMS error of SST around the demise of the ISM.

The evolution of the kinetic energy of the 850 hPa winds centred around the onset of the ISM (Figure 10) indicates the growing strength of the Somali Jet in the western part of the domain. It matures to higher wind speeds well past the onset date (day +15 and beyond) unlike the analysis (around day +10; Noska and Misra, 2016). It may be noted that the spatial correlation of the kinetic energy prior to onset are much weaker than after onset, when the circulation becomes stronger (and organized) by the establishment of the monsoon trough and associated

atmospheric convection. Notably the RMS error grows from its pre-onset values into the post-onset period as well (Figure 10). Therefore, the organized and stronger 850 hPa winds in the post-onset period has an impact on the wind driven surface ocean currents, which have a significant role to play in the modulation of the SST (Schott and McCreary, 2001). This explains the improved spatial coherence of the simulated SST from the RCOAM simulation in the post-onset period (Figure 8) than around the demise date (Figure 9) when the Somali Jet is weaker. This is further substantiated in Figure 11, which shows that the Somali Jet weakens almost a month before the demise date and the kinetic energy is well below 25 $m^{-2}s^{-2}$ over most of the Indian Ocean in the domain. The spatial correlation (RMS error) is much higher (lower) centred around the demise date (Figure 11) compared with the period around the onset date of the ISM (Figure 10).

Another robust feature of the seasonal evolution of the ISM is the reversal of the temperature gradient at 300 hPa (Rai Sircar and Patil, 1961; Yanai *et al.*, 1992). Yanai *et al.* (1992) noted a reversal of the meridional temperature gradient at 300 hPa computed roughly across 5° and 25°N latitudes. Noska and Misra (2016) showed that this reversal of temperature gradient quite nicely followed their definition of onset and demise based on the all India monsoon rainfall index. We have similarly plotted the east-west progression of the reversal of the temperature gradient at different lead/lag with respect to the onset date of the ISM (Figure 12(a) and (b)) diagnosed from the all India monsoon rain index following Noska and Misra (2016). The temperature gradient reversal at around 60°E coincides roughly with the onset date of the ISM both in the MERRA-2 (Figure 12(a)) and the RCOAM model simulation (Figure 12(b)). Similarly, we observe that the reversal of the temperature gradient at around 57°E in MERRA-2 (Figure 12(c)) coincides with the demise date of the ISM, which is also similar in the RCOAM simulation (Figure 12(d)). It should be noted that Goswami and Xavier (2005) suggest that the reversal of the temperature gradient at the time of onset of the ISM also coincides with the triggering of the moist symmetric instability. They explain this coincidence with the fact that the large-scale heating gradient initiated by the elevated heating of the Tibetan plateau results in large-scale cyclonic vorticity in the lower troposphere, which forces the zero line of the absolute vorticity to shift north of the equator, making conditions conducive for moist symmetric instability.

4.3. Intraseasonal variability

The climatological mean variance of the 20–90 days filtered precipitation anomalies from TRMM and the RCOAM simulation is shown in Figure 13. These anomalies were filtered using the first order Butterworth Filter (Krishnamurti and Subrahmanyam, 1995). In a broad sense, the observed high intra-seasonal variance along the Malabar Coast, Indo-Gangetic Plains, and over northeastern part of India including Bangladesh is reasonably captured by the RCOAM simulation. However, there are distinct disparities including the low variance exhibited

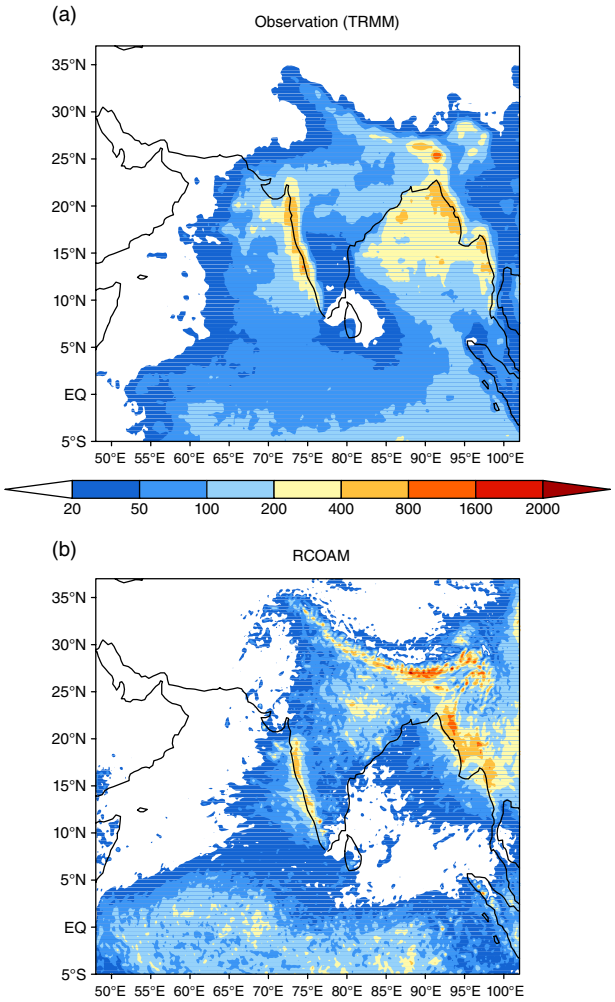

Figure 13. Intraseasonal variance of precipitation (20–90 days bandpass filtered using first order Butterworth filter) from (a) observations (TRMM), (b) RCOAM simulation for the ISM season. Units are in mm day^{-2}. [Colour figure can be viewed at wileyonlinelibrary.com].

by the RCOAM simulation over the Bay of Bengal, the western Arabian Sea, and over parts of northwestern India. Furthermore, the variance over the Indo-Gangetic Plains, equatorial Indian Ocean, and over Southeast Asia is overestimated in the RCOAM simulation. Some of this bias could be explained by the cold SST bias displayed by the model over the Bay of Bengal (Figure 2(d)) that is likely to undermine convective rainfall (McBride and Fraedrich, 1995).

In addition, we show the composite picture of the active and break spells of the intraseasonal oscillation of the ISM (Figure 14). The active (break) spells for each ISM season over the simulation period of RCOAM was determined by isolating periods of 5 successive days of the 20–90 day filtered positive (negative or zero) precipitation anomalies over Central India (15°–25°N and 75°–85°E; Goswami and Xavier, 2003; Umakant *et al.*, 2015) for both the model simulation and from TRMM observations. The filtered 20–90-day 850 hPa wind anomalies were similarly composited based on the intraseasonal precipitation anomalies over Central India from the model simulation and CFSR.

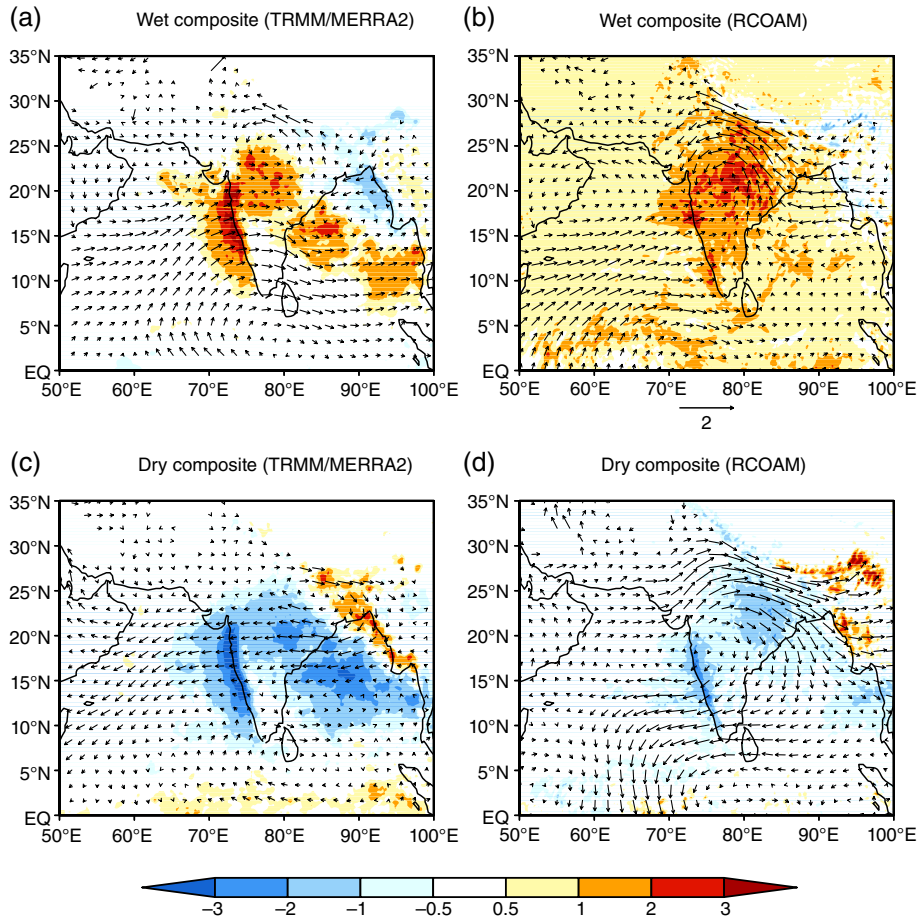

Figure 14. Composite band pass filtered (20–90 days) 850 hPa winds (ms^{-1}) overlaid with precipitation anomalies ($mm\,day^{-1}$) for wet spell from (a) TRMM3B42 (rainfall) and MERRA2 (850 hPa winds) and (b) RCOAM simulation. Similarly, composites for dry spell from (c) TRMM3B42 (rainfall) and MERRA2 (850 hPa winds) and (d) RCOAM simulation. [Colour figure can be viewed at wileyonlinelibrary.com].

Figure 14 indicates that the active and break composites from the RCOAM simulation are reasonably well captured when compared with the corresponding observations. The active spell is characterized by 850 hPa wind anomalies that reinforce the climatological southwesterly flow across the sub-continent and the establishment of monsoon low over Central India (Krishnamurti *et al.*, 1992) as seen in the observations (Figure 14(a)) is represented reasonably well in the RCOAM simulation (Figure 14(b)). It may be noted, however, that the intraseasonal precipitation anomalies over the Bay of Bengal in the RCOAM simulation is comparatively weak (Figure 14(b)). Similarly, the dry spell of the intraseasonal oscillation of the ISM is characterized by anomalous flow that weakens the climatological flow of the ISM with negative (positive) precipitation anomalies over Central India (foothills of the Himalayas; Sikka and Gadgil, 1980; Figure 14(c)). Again, the RCOAM simulation depicts these features with the anomalies over the Bay of Bengal being rather weak (Figure 14(d)).

4.4. Interannual variations

As noted in Noska and Misra (2016) the length of the ISM season has an important bearing on the interannual variability. It was shown in their observational study that long (short) seasons are associated with anomalous wet (dry) ISM seasonal rainfall anomalies. This is also reconfirmed in the shorter period of the RCOAM simulation period (1990–2007) from the correlations shown between the seasonal rainfall anomalies of ISM and the length of the season (Figure 15(a) and (b)). Furthermore, it is seen that early (later) onset of the ISM season usually coincides with the wetter (drier) seasonal rainfall anomalies (Figure 15(c) and (d)). Similarly, later (early) demise of the ISM usually coincides with anomalous wet (dry) seasonal rainfall anomalies (Figure 15(e) and (f)). A part of this relationship in Figure 15 is realized by the teleconnection of the onset date variations of ISM with ENSO variability (Noska and Misra, 2016; Figure 16(a) and (c)). A warm (cold) ENSO event in December–January–February (DJF) is followed by late (early) onset of the ISM. Similarly, the early (later) demise of the ISM is associated with positive (negative) ENSO anomalies in the east Pacific that coincides with the positive (negative) anomalies of western (eastern) Indian Ocean (Figure 16(b) and (d)) in the near contemporaneous September–October–November (SON) season. Similarly, the total seasonal rainfall anomaly of the ISM is related to the ENSO anomalies of the preceding DJF season (Figure 16(e) and (g)) and near succeeding SON season (Figure 16(f) and (h)). It should be noted that in the observational panels (Figure 16(b) and (f)) the correlations over

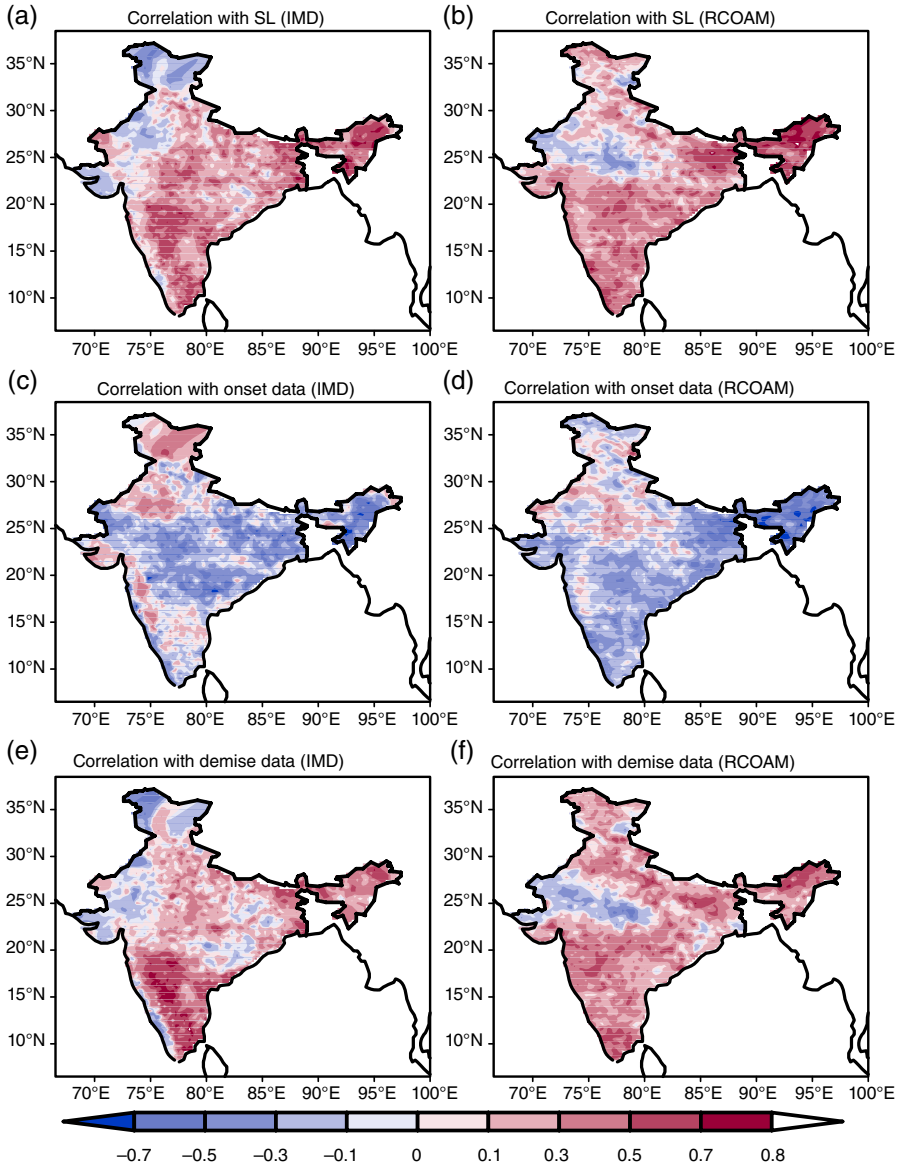

Figure 15. The correlation of seasonal anomalies of all India averaged rainfall with length of the ISM season from (a) IMD and (b) RCOAM. The correlation of onset date of ISM season with the succeeding seasonal anomalies of ISM rainfall from (c) IMD and (d) RCOAM. Similarly, the correlation of the demise date of the ISM season with the preceding seasonal anomalies of ISM rainfall form (e) IMD and (f) RCOAM. [Colour figure can be viewed at wileyonlinelibrary.com].

the eastern equatorial Pacific Ocean is not as significant as the RCOAM simulation. However, the manifestation of the Indian Ocean anomalies and their relation to the ISM seasonal rainfall and length anomalies in Figure 16(b) and (f) correspond to the ENSO forcing of the tropical Indian Ocean (Krishnamurthy and Kirtman, 2003).

5. Conclusions

This regional-coupled ocean–atmosphere modelling study of the Indian Summer Monsoon (ISM) is uniquely placed in that the coupled system is forced at the lateral boundaries with realistic boundary conditions of the ocean and atmosphere. Some of the earlier studies of the ISM simulations with the regional-coupled ocean–atmosphere model have been forced with climatological monthly mean boundary conditions of temperature and salinity and in addition have nudged the surface salinity (VenkataRatnam *et al.*, 2009; Samala *et al.*, 2013), which the current study avoids. Although the experimental setup and model resolutions of the few regional-coupled ocean–atmosphere studies of the ISM (Table 2) are different from the RCOAM simulation presented in this paper, there are some encouraging signs of improving ISM simulation using high-resolution regional models. Majority of these studies suggest that high-resolution air–sea coupling reduces the SST and precipitation bias, improves intraseasonal variations relative to their uncoupled version.

We have conducted a comprehensive validation of the 18-year Regional-Coupled Ocean–Atmosphere Model (RCOAM) that included surface and upper air atmospheric variables and surface and upper ocean variables. We have

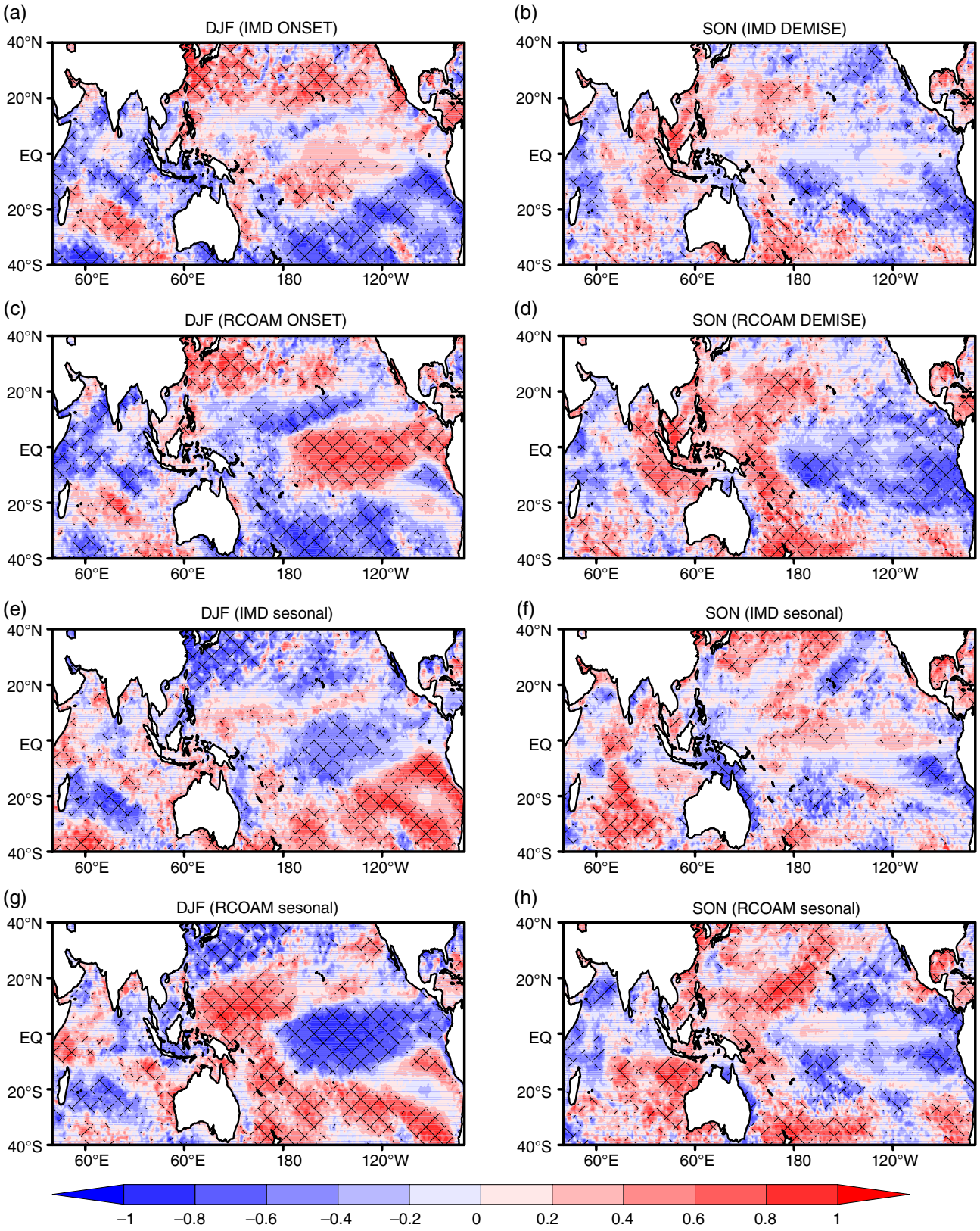

Figure 16. The correlation of mean DJF SST anomalies from observations with onset date of ISM from (a) IMD rainfall dataset and (c) RCOAM simulation. The correlation of mean SON SST anomalies from observations with demise date of ISM from (b) IMD rainfall dataset and (d) RCOAM simulation. The correlation of mean DJF SST anomalies from observations with seasonal rainfall anomalies of ISM from (e) IMD rainfall dataset and (g) RCOAM simulation. (f and h) Same as (e) and (g) but with mean SON SST anomalies. The hatched regions are significant at 90% confidence interval by the bootstrapping technique. [Colour figure can be viewed at wileyonlinelibrary.com].

shown that the robust seasonal variation of the ISM rainfall both in the observations and model simulation is accompanied by associated changes in the meridional upper air temperature gradient, low level changes in kinetic energy, SST changes, and meridional ocean heat transport. These changes signify the true coupled ocean–atmosphere phenomenon of the ISM. The RCOAM simulation of this study capture the transitions happening in the regional atmosphere and ocean across the onset and demise time of the ISM.

The RCOAM simulation also captures the intra-seasonal variations of the ISM with dry (wet) spells ascertained in the rainfall anomalies coinciding with anomalous counteracting (enhancing) low level climatological monsoon circulations. In the wet spell the intra-seasonal monsoon trough is well established and centred over central India while during the dry spell, the anomalous flow is easterly in central India and northwesterly over northeast India. The interannual variations also show that the seasonal length of the ISM has an important bearing on the seasonal rainfall anomalies. This variation is shown to tie with the ENSO variations in the east Pacific. However, despite these encouraging results it was noted that the systematic bias in surface fluxes, cloud fraction, SST, and precipitation of the RCOAM simulation provides considerable scope for improvement notwithstanding the uncertainties in the observational analysis of these variables. Further work is ongoing to understand the impact of air-sea coupling on the RCOAM simulation of the seasonal transition of the ISM.

Acknowledgements

The authors gratefully acknowledge the financial support given by the Earth System Science Organization, Ministry of Earth Sciences, Government of India (Grant number MM/SERP/FSU/2014/SSC-02/002) to conduct this research under Monsoon Mission. We thank the Indian Meteorological Department for the availability of the daily rain analysis over India. The supercomputing facility provided by XSEDE under grant number ATM10010 was used to complete the model integrations used in this study.

References

Adler RF, Huffman GJ, Bolvin DT, Curtis S, Nelkin EJ. 2000. Tropical rainfall distributions determined using TRMM combined with other satellite and rain gauge information. *J. Appl. Meteorol.* **39**(12): 2007–2023, doi: 10.1175/1520-0450(2001)040<2007:TRDDUT>2.0.CO;2.

Alpert S, Hanahan D, Teitelman G. 1988. Hybrid insulin genes reveal a developmental lineage for pancreatic endocrine cells and imply a relationship with neurons. *Cell* **53**: 295–308.

Ananthakrishnan R, Soman MK. 1988. The onset of south-west monsoon over Kerala: 1901–1980. *J. Climatol.* **8**(3): 283–296, doi: 10.1002/joc.3370080305.

Ananthakrishnan R, Srinivasan V, Ramakrishnan AR, Jambunathan R. 1968. Synoptic features associated with onset of southwest monsoon over Kerala. India Metorological Department, Forecasting Manual Unit Report No. IV-18.2. India

Bhaskaran B, Jones RG, Murphy JM, Noguer M. 1996. Simulations of the Indian summer monsoon using a nested regional climate model: domain size experiments. *Clim. Dyn.* **12**: 573–587.

Bollasina MA, Ming Y. 2013. The role of land-surface processes in modulating the Indian monsoon cycle. *Clim. Dyn.* **41**: 2497–2509.

Bordoni S, Schneider T. 2008. Monsoons as eddy-mediated regime transitions of the tropical overturning circulation. *Nat. Geosci.* **1**: 515–519, doi: 10.1038/ngeo248.

Carton JA, Giese BS. 2008. A reanalysis of ocean climate using simple ocean data assimilation (SODA). *Mon. Weather Rev.* **136**: 2999–3017, doi: 10.1175/2007MWR1978.1.

Chaudhari HS, Pokhrel S, Saha SK, Dhakate A, Yadav RK, Salunke K, Mahapatra S, Sabeerali CT, Suryachandra AR. 2013. Model biases in long coupled runs of NCEP CFS in the context of Indian summer monsoon. *Int. J. Climatol.* **33**: 1057–1069, doi: 10.1002/joc.3489.

Chirokova G, Webster PJ. 2006. Interannual variability of Indian Ocean heat transport. *J. Clim.* **19**: 1013–1031.

Chou M-D, Suarez MJ. 1994. An efficient thermal infrared radiation parameterization for use in general circulation models. Technical report series on global modeling and data assimilation, NASA/TM-1994-104606, vol. 3, 85 pp. Greenbelt, MD

Chou M-D, Lee K-T, Tsay S-C, Fu Q. 1996. Parameterization for cloud long wave scattering for use in atmospheric models. *J. Clim.* **12**: 159–169.

Conkright ME, Locarnini RA, Garcia HE, O'Brien TD, Boyer TP, Stephens C, Antonov JJ. 2002. World ocean atlas 2001: Objective analysis, data statistics, and figs: CD-ROM documentation. National Oceanographic Data Center Internal Report No. 17, 21 pp. USA

Dash SK, Shekhar MS, Singh GP. 2006. Simulation of Indian summer monsoon circulation and rainfall using RegCM3. *Theor. Appl. Climatol.* **86**: 161–172.

Delworth TL, Manabe S. 1988. The influence of potential evaporation on the variabilities of simulated soil wetness and climate. *J. Clim.* **1**: 523–547.

Dinku T, Connor S, Ceccato P. 2010. Comparison of CMORPH and TRMM-3B42 over mountainous regions of Africa and South America. In *Satellite Rainfall Applications for Surface Hydrology*, Gebremichael M, Hossain F (eds). Springer: The Netherlands, 193–204.

Donlon CJ, Martin M, Stark JD, Roberts-Jones J, Fiedler E, Wimmer W. 2011. The operational sea surface temperature and sea ice analysis (OSTIA). *Remote Sens. Environ.* **116**, 140–158, doi: 10.1016/j.rse.2010.10.017.

Drbohlav HKL, Wang B. 2005. Mechanism of the northward-propagating intraseasonal oscillation: insights from a zonally symmetric model. *J. Clim.* **18**: 952–972.

Ek M, Mitchell KE, Lin Y, Rogers E, Grunmann P, Koren V, Gayno G, Tarpley JD. 2003. Implementation of Noah land-surface model advances in the NCEP operational Mesoscale Eta model. *J. Geophys. Res.* **108**: 8851, doi: 10.1029/2002JD003296.

Gadgil S, Sajani S. 1998. Monsoon precipitation in the AMIP runs. *Clim. Dyn.* **14**: 659–689.

Goswami BN, Sengupta D. 2003. A note on the deficiency of NCEP/NCAR reanalysis surface winds over the equatorial Indian Ocean. *J. Geophys. Res.* **108**: 3124, doi: 10.1029/2002JC001497.

Goswami BN, Xavier PK. 2003. Potential predictability and extended range prediction of Indian summer monsoon breaks. *Geophys. Res. Lett.* **30**(18): 1966, doi: 10.1029/200 3GL017.810.2003.

Goswami BN, Xavier PK. 2005. ENSO control on the south Asian monsoon through the length of the rainy season. *Geophys. Res. Lett.* **32**: L18717, doi: 10.1029/2005GL023216.

Habib E, Krajewski WF. 2002. Uncertainty analysis of the TRMM ground-validation radar-rainfall products: application to the TEFLUN-B Field campaign. *J. Appl. Meteorol.* **41**: 558–572.

Haidvogel DB, Blanton J, Kindle JC, Lynch DR. 2000. Coastal ocean modeling: processing and real-time systems. *Oceanography* **13**: 35–46.

Han W, Vialard J, McPhaden MJ, Lee T, Masumoto Y, Feng M, De Ruijter WPM. 2014. Indian Ocean decadal variability. *Bull. Am. Meteorol. Soc.* **43**: 1679–1703.

Hong S-Y, Pan H-L. 1996. Nonlocal boundary layer vertical diffusion in a medium-range forecast model. *Mon. Weather Rev.* **122**: 3–26.

Huffman GJ, Adler RF, Rudolf B, Schneider U, Keehn PR. 1995. Global precipitation estimates based on a technique for combining satellite-based estimates, rain gauge analysis, and NWP model precipitation information. *J. Clim.* **8**(5): 1284–1295.

Huffmann GJ and coauthors. 1997. The TRMM Multisatellite Precipitation Analysis (TMPA): Quasi-Global, Multiyear, Combined-Sensor Precipitation Estimates at Fine Scales. *J. Hydromet.* **8**: 38–55.

Ji Y, Vernekar AD. 1997. Simulation of the Asian monsoons of 1987 and 1988 with a regional model nested in a global GCM. *J. Clim.* **10**: 1965–1979.

Juang H-MH, Kanamitsu M. 1994. The NMC nested regional spectral model. *Mon. Weather Rev.* **122**: 3–26.

Kalnay E, Kanamitsu M, Kistler R, Collins W, Deaven D, Gandin L, Iredell M, Saha S, White G, Woollen J, Zhu Y, Leetmaa A, Reynolds B, Chelliah M, Ebisuzaki W, Higgins W, Janowiak J, Mo KC, Ropelewski C, Wang J, Jenne R, Joseph D. 1996. The NCEP/NCAR 40-year reanalysis project. *Bull. Am. Meteorol. Soc.* **77**: 437–472.

Kanamitsu M, Ebusuzaki W, Woollen J, Yang S-K, Hnilo J, Fiorino M, Potter GL. 2002. NCEP-DOE AMIP-II reanalysis (R-2). *Bull. Am. Meteorol. Soc.* **83**: 1631–1643.

Kanamitsu M, Yoshimura K, Yhang Y, Hong S. 2010. Errors of interannual variability and trend in dynamical downscaling of reanalysis. *J. Geophys. Res.* **115**: D17115, doi: 10.1029/2009JD013511.

Kim H-M, Webster PJ, Curry JA, Toma VE. 2012. Asian summer monsoon prediction in ECMWF system 4 and NCEP CFSv2 retrospective seasonal forecasts. *Clim. Dyn.* **39**: 2975–2991. doi: 10.1007/s00382-012-1470-5.

Kim D, Lee M-I, Kim D, Schubert SD, Waliser DE, Tian B. 2014. Representation of tropical subseasonal variability of precipitation in global reanalyses. *Clim. Dyn.* **43**: 517–534.

Koster RD, Dirmeyer PA, Guo Z, Bonan G, Chan E, Cox P, Gordon CT, Kanae S, Kowalczyk E, Lawrence D, Liu P, Lu CH, Malyshev S, McAvaney B, Mitchell K, Mocko D, Oki T, Oleson K, Pitman A, Sud YC, Taylor CM, Verseghy D, Vasic R, Xue Y, Yamada T, GLACE Team. 2004. Regions of strong coupling between soil moisture and precipitation. *Science* **305**: 1138–1140.

Koteswaram P. 1958. The easterly jet stream in the tropics. *Tellus* **10**(1): 43–57.

Krishnamurthy V, Kirtman B. 2003. Variability of the Indian Ocean: relation to monsoon and ENSO. *Q. J. R. Meteorol. Soc.* **129**: 1623–1646.

Krishnamurti TN, Ramanathan Y. 1982. Sensitivity of the monsoon onset to differential heating. *J. Atmos. Sci.* **39**: 1290–1306.

Krishnamurti TN, Subrahmanyam D. 1995. The 30–50 day mode at 850 mb during MONEX. *J. Atmos. Sci.* **39**: 2088–2095.

Krishnamurti TN, Sinha MC, Krishnamurti R, Oosterhof D, Comeaux J. 1992. Angular momentum, length of day and monsoon allow frequency mode. *J. Meteorol. Soc. Jpn.* **70**: 131–166.

Large WG, McWilliams JC, Doney SC. 1994. Oceanic vertical mixing: a review and a model with a nonlocal boundary layer parameterization. *Rev. Geophys.* **32**(4): 363–403, doi: 10.1029/94RG01872.

Li H, Misra V. 2014. Thirty-two year ocean–atmosphere coupled downscaling ofglobal reanalysis over the Intra-American Seas. *Clim. Dyn.* **43**(9): 2471–2489, doi: 10.1007/s00382-014- 2069–9.

Li H, Kanamitsu M, Hong S-Y. 2012. California reanalysis downscaling at 10 km using an ocean–atmosphere coupled regional model system. *J. Geophys. Res. Atmos.* **117**: D12118, doi: 10.1029/2011JD017372.

Li H, Kanamitsu M, Hong S-Y, Yoshimura K, Cayan DR, Misra V. 2013. A high-resolution ocean–atmosphere coupled downscaling of the present climate over California. *Clim. Dyn.* **42**: 701–714. doi: 10.1007/s00382-013- 1670–7.

Li H, Kanamitsu M, Hong S-Y, Yoshimura K, Cayan DR, Misra V, Sun L. 2014. Projected climate change scenario over California by a regional ocean–atmosphere coupled model system. *Clim. Change* **122**(4): 609–619, doi: 10.1007/s10584-013- 1025–8.

Lucas-Picher P, Christensen JH, Saeed F, Kumar P, Asharaf S, Ahrens B, Wiltshire AJ, Jacob D, Hagemann S. 2011. Can regional climate models represent the Indian monsoon? *J. Hydrometerol.* **12**: 849–868.

McBride JL, Fraedrich K. 1995. CISK: a theory for the response of tropical convective complexes to variations in sea surface temperature. *Q. J. R. Meteorol. Soc.* **121**: 783–796.

Mellor GL, Yamada T. 1982. Development of a turbulence closure model for geophysical fluid problems. *Rev. Geophys. Space Phys.* **20**: 851–875.

Misra V. 2008. Coupled interactions of the monsoons. *Geophys. Res. Lett.* **35**: 1–7.

Misra V, Li H. 2013. The seasonal predictability of the Asian summer monsoon in a two tiered forecast system. *Clim. Dyn.* **42**: 2491–2507. doi: 10.1007/s00382-013- 1838–1.

Misra V, Mishra A. 2016. The oceanic influence on the rainy season of peninsular Florida. *JGR-Atmosphere* **121**: 7691–7709. doi: 10.1002/2016JD025002.

Misra V, Mishra A, Li H. 2016. The sensitivity of the regional coupled ocean atmosphere simulations over the Intra-Americas Seas to the prescribed bathymetry. *Dyn. Atm. and Ocean*, doi: 10.1016/j.dynatmoce.2016.08.007.

Monterey GI, Levitus S. 1997. Climatological cycle of mixed layer depth in the world ocean. U.S. Government Printing Office, NOAA NESDIS: Maryland, 5.

Moorthi S, Suarez MJ. 1992. Relaxed Arakawa-Schubert, a parameterization of moist convection for general-circulation models. *Mon. Weather Rev.* **120**: 978–1002.

Noska R, Misra V. 2016. Characterizing the onset and demise of the Indian Summer Monsoon Geophys. *Res. Lett.* **43**: 4547–4554. doi: 10.1002/2016GL068409.

Pai DS, Sridhar L, Badwaik MR, Rajeevan M. 2014. Analysis of the daily rainfall events over India using a new long period (1901–2010) high resolution ($0.25° \times 0.25°$) gridded rainfall data set. *Clim. Dyn.* **45**(3–4): 755–766. doi: 10.1007/s00382-014-2307-1.

Rai Sircar NC, Patil CD. 1961. Horizontal distribution of temperature over India in May during years of early, normal, and late southwest monsoon. *Indian J. Meteorol. Geophys.* **12**: 377–381.

Ramu DA, Sabeerali CT, Chattopadhyay R, Rao DN, George G, Dhakate AR, Salunke K, Srivastava A, Rao SA. 2016. Indian summer monsoon rainfall simulation and prediction skill in the CFSv2 coupled model: impact of horizontal resolution. *J. Geophys. Res. Atmos.* **121**: 2205–2221, doi: 10.1002/2015JD024629.

Reichle RH, Liu Q. 2014. Observation-corrected precipitation estimates in GEOS-5. NASA/TM-2014-104606, vol. 35. Greenbelt, MD.

Reynolds RW, Smith TM, Liu C, Chelton DB, Casey KS, Schlax MG. 2007. Daily high-resolution-blended analyses for sea surface temperature. *J. Clim.* **20**(22): 5473–5496, doi: 10.1175/2007JCLI 1824.1.

Reynolds RW, Gentemann CL, Corlett GK. 2010. Evaluation of AATSR and TMI satellite SST data. *J. Clim.* **23**: 152–165.

Rossow WB, Schiffer RA. 1999. Advances in understanding clouds from ISCCP. *Bull. Am. Meteorol. Soc.* **80**: 2261–2288.

Saeed F, Hagemann S, Jacob D. 2009. Impact of irrigation on the South Asian summer monsoon. *Geophys. Res. Lett.* **36**: L20711.

Saeed F, Hagemann S, Jacob D. 2012. A framework for the evaluation of the South Asian summer monsoon in a regional climate model applied to REMO. *Int. J. Climatol.* **32**: 430–440. doi: 10.1002/joc.2285 (in press).

Saha S, Moorthi S, Pan H-L, Wu X, Wang J, Nadiga S, Tripp P, Kistler R, Woollen J, Behringer D, Liu H, Stokes D, Grumbine R, Gayno G, Wang J, Hou Y-T, Chuang H-Y, Juang H-MH, Sela J, Iredell M, Treadon R, Kleist D, Van Delst P, Keyser D, Derber J, Ek M, Meng J, Wei H, Yang R, Lord S, Van Den Dool H, Kumar A, Wang W, Long C, Chelliah M, Xue Y, Huang B, Schemm J-K, Ebisuzaki W, Lin R, Xie P, Chen M, Zhou S, Higgins W, Zou C-Z, Liu Q, Chen Y, Han Y, Cucurull L, Reynolds RW, Rutledge G, Goldberg M. 2010. The NCEP climate forecast system reanalysis. *Bull. Am. Meteorol. Soc.* **91**: 1015–1057, doi: 10.1175/2010BAMS3001.1.

Samala BK, Nagaraju C, Banerjee S, Kaginalkar A, Dalvi M. 2013. Study of Indian summer monsoon using WRF-ROMS regional coupled model simulations. *Atmos. Sci. Lett.* **14**: 20–27.

Schott FA, McCreary JP Jr. 2001. The monsoon circulation of the northern Indian Ocean. *Prog. Oceanogr.* **51**(1): 1–123.

Seo H, Miller AJ, Roads JO. 2007. The Scripps coupled ocean–atmosphere regional (SCOAR) model, with applications in the Eastern Pacific Sector. *J. Clim.* **20**: 381–402.

Seo H, Murtugudde R, Jochum M, Miller AJ. 2008. Modeling of mesoscale coupled ocean–atmosphere interaction and its feedback to ocean in the Western Arabian Sea. *Ocean Model.* **25**: 120–131.

Seo H, Xie S-P, Murtugudde R, Jochum M, Miller AJ. 2009. Seasonal effects of Bay of Bengal barrier layer dynamics in a regional coupled model. *J. Clim.* **22**: 6577–6596.

Shchepetkin AF, McWilliams JC. 2005. The Regional Ocean Modeling System: a split-explicit, free-surface, topography following coordinates ocean model. *Ocean Model.* **9**: 347–404.

Sperber KR, Palmer TN. 1996. Interannual tropical rainfall variability in general circulation model simulations associated with the Atmospheric Model Intercomparison Project. *J. Clim.* **9**: 2727–2750.

Sperber KR, Brankovic C, Déqué M, Frederiksen CS, Graham R, Kitoh A, Kobayashi C, Palmer T, Puri K, Tennant W, Volodin E. 2001. Dynamical seasonal predictability of the Asian summer monsoon. *Mon. Weather Rev.* **129**: 2226–2248.

Suarez M, Bacmeister J. 2015. Development of the GEOS-5 atmospheric general circulation model: evolution from MERRA to MERRA2. *Geosci. Model Dev.* **8**: 1339–1356, doi: 10.5194/gmd-8-1339-2015.

Tiedtke M. 1983. The sensitivity of the time-mean large-scale flow to cumulus convection in the ECWMF model. *In: Proceedings of ECMWF Workshop on Convection in Large-Scale Models*. European Centre for Medium-Range Forecasts, Reading, UK, pp 297–316.

Umakant U, Kesarkar AP, Raju A, VijayaBhaskar Rao S. 2015. Representation of monsoon intraseasonal oscillations in regional climate model: sensitivity to convective physics. *Clim. Dyn.* **47**: 895–912. doi: 10.1007/s00382-015-2878-5.

Umlauf L, Burchard H. 2003. A generic length-scale equation for geophysical turbulence models. *J. Mar. Res.* **61**: 235–265.

Valcke S. 2006. OASIS3 User Guide (oasis3 prism 2-5), PRISM Support Initiative Report No 3. 15 CERFACS, Toulouse, France, 64 pp.

VenkataRatnam J, Krishna Kumar K. 2005. Sensitivity of the simulated monsoons of 1987 and 1988 to convective parameterization schemes in MM5. *J. Clim.* **18**: 2724–2743.

VenkataRatnam J, Giorgi F, Kaginalkar A, Cozzini S. 2009. Simulation of the Indian monsoon using the RegCM3–ROMS regional coupled model. *Clim. Dyn.* **33**: 119–139.

Wang B, Ding Q, Fu X, Kang I-S, Jin K, Shukla J, Doblas-Reyes F. 2005. Fundamental challenge in simulation and prediction of summer monsoon rainfall. *Geophys. Res. Lett.* **32**: L15711, doi: 10.1029/2005GL022734.

Ward E, Buytaert W, Peaver L, Wheater H. 2011. Evaluation of precipitation products over complex mountainous terrain: a water resources perspective. *Adv. Water Resour.* **34**: 1222–1231, doi: 10.1016/j.advwatres.2011.05.007.

Wargan K, Coy L. 2016. Strengthening of the tropopause inversion layer during the 2009 sudden stratospheric warming: a MERRA-2 study. *J. Atmos. Sci.* **73**: 1871–1887, doi: 10.1175/JAS-D-15-0333.1.

Webster PJ. 2000. The coupled monsoon system. In *The Asian Monsoon*, Wang B (ed). Springer.

Webster P, Chou LC. 1980. Seasonal structure of a simple monsoon system. *J. Atmos. Sci.* **37**: 354–367.

Webster PJ, Magana VO, Palmer TN, Shukla J, Tomas RA, Yanai M, Yasunari T. 1998. Monsoons: processes, predictability, and the prospects for prediction. *J. Geophys. Res.* **103**: 14451–14510.

Wu R, Kirtman BP. 2005. Role of Indian and Pacific Ocean air-sea coupling in tropical atmospheric variability. *Clim. Dyn.* **25**: 155–170.

Wyrtki K. 1971. *Oceanographic Atlas of the International Indian Ocean Expedition*. National Science Foundation: Washington, DC, 531 pp.

Yanai M, Li C, Song Z. 1992. Seasonal heating of the Tibetan Plateau and its effects on the evolution of the Asian summer monsoon. *J. Meteorol. Soc. Jpn.* **70**: 319–351.

Yu L, Jin X, Weller RA. 2008. Multidecade Global Flux Datasets from the Objectively Analyzed Air-sea Fluxes (OAFlux) Project: Latent and sensible heat fluxes, ocean evaporation, and related surface meteorological variables. OAFlux Project Technical Report No. OA-2008-01, Woods Hole Oceanographic Institution, Woods Hole, MA, 64 pp.

Zawadzki I. 1975. On radar-raingage comparison. *J. Appl. Meteorol.* **14**: 1430–1436.

Zou L, Zhou T. 2016. A regional ocean–atmosphere coupled model developed for CORDEX East Asia: assessment of Asian summer monsoon simulation. *Clim. Dyn.* **12**: 3627–3640.

Zulkafli Z, Buytaert W, Onof C, Manz B, Tarnavsky E, Lavado W, Guyot J-L. 2014. A comparative performance analysis of TRMM 3B42 (TMPA) versions 6 and 7 for hydrological applications over Andean-Amazon River Basins. *J. Hydrometerol.* **15**: 581–592.

